Chair of Structural and Functional Ceramics

Master's Thesis

Varistor Grain Boundary Characterization by High Resolution Analytics

Johanna Luise Byloff, BSc

March 2022

Eidesstattliche Erklärung:
Ich erkläre an Eides statt, dass ich diese Arbeit selbständig verfasst, andere als die angegebenen Quellen und Hilfsmittel nicht benutzt und mich auch sonst keiner unerlaubten Hilfsmittel bedient habe.

Affidavit:
I declare in lieu of oath, that I wrote this thesis and performed the associated research myself, using only literature cited in this volume.

Datum Unterschrift

Acknowledgements

First and foremost, I would like to sincerely thank my supervisor Ao. Univ.-Prof. Peter Supancic for giving me the opportunity to write my master's thesis on such an engaging and challenging topic. I am very grateful for his support and understanding regarding the theoretical foundations of my thesis and his precise and astute input on my written work.

Secondly, but not in any way less, a heartfelt thank you goes out to Dr. Francisca Mendez-Martin, who not only supervised my experimental work and introduced me to most of the methods employed in this thesis, but sacrificed early mornings, late evenings and whole weekends to help me obtain my experimental results. Without her encouragement, kindness and patience I would not have succeeded in putting these very challenging techniques into practice.

I would like to thank DI Thomas Billovits for the training and assistance he provided me with regarding the electrical measurements in my thesis. Additionally, I thank my colleagues at the institute for physical metallurgy, DI Andreas Rosenauer and Daniel Rainer, BSc, for providing me with emotional and technical support when there were issues with my measurements.

I gratefully acknowledge the financial support under the scope of the COMET program within the K2 center "Integrated Computational Material, Process and Product Engineering (IC-MPPE)" (Project No. 859480). This program is supported by the Austrian Federal Ministries for Transport, Innovation and Technology (BMVIT) and for Digital and Economic Affairs (BMDW), represented by the Austrian research funding association (FFG) and the federal states of Styria, Upper Austria and Tyrol.

Last but not least I would like to warmly thank Dr. Sarah Kettner, who encouraged me to continue my course of studies at this university, especially during my first year, and has supported me since my beginnings in Leoben. Without her choir, her cultural projects and her endless encouragement and optimism I would not be where I am today.

Contents

Abstract

Abstract

A novel method for the characterization of complementary parameters of single varistor grain boundaries is proposed. Therein, electrical parameters (Current-Voltage (I-V) characteristic), microstructural parameters (Electron Backscatter Diffraction (EBSD) scan), and the chemical composition (Atom Probe Tomography (APT), via a Focused Ion Beam (FIB) Lift-Out) are measured. Electrical measurements of different grain boundaries are analysed and categorized according to their grain boundary misorientation. APT scans of bulk material, a parameter study as well as two complete characterizations of grain boundaries are presented. I-V characteristics show asymmetry depending on the polarity of the interface. Concentration profiles of comprised elements are shown and an asymmetrical oxygen-zinc profile is showcased for both grain boundaries. APT measurements show heightened bismuth concentration in the grain boundary. Cobalt only shows a peak in concentration in the grain boundary with an asymmetrical I-V characteristic, all other dopant elements show uniform behaviour for both grain boundaries.

Zusammenfassung

Eine neue Methode für die Charakterisierung von komplementären Kenngrößen einzelner Varistorkorngrenzen wird vorgestellt. Diese umfasst die Erfassung elektrischer Kenngrößen (Strom-Spannung (I-U) Kennlinien), Gefügeparametern (Electron Backscatter Diffraction (EBSD) Scans), und der chemischen Zusammensetzung (Atomsondentomographie (APT) via einem Focused Ion Beam (FIB) Lift-Out). Elektrische Messungen verschiedener Korngrenzen werden analysiert und je nach ihrer Korngrenzenmisorientierung kategorisiert und diskutiert. APT Scans von Proben, die den Körnern entnommen worden sind, eine Parameterstudie sowie zwei vollständige Charakterisierungen von Korngrenzen werden präsentiert. I-U Kennlinien zeigen Asymmetrie abhängig von der Polarität an der Korngrenze. Konzentrationsprofile von enthaltenen Elementen werden gezeigt sowie eine asymmetrische Verteilung von Zink und Sauerstoff an der Korngrenze wird festgestellt. APT Messungen zeigen eine erhöhte Wismuth-Konzentration in der Korngrenze. Cobalt zeigt nur eine erhöhte Konzentration in der Korngrenze mit einer asymmetrischen I-U Kennlinie, alle anderen Dotierelemente zeigen gleichförmige Eigenschaften für beide Korngrenzen.

Chapter 1

Introduction

Metal oxide varistors are electroceramic components composed of ZnO as well as metal oxide dopants that have nonlinear ampere-volt (I-V) characteristics. At low voltages, they show high resistance, while at high voltages, after a certain switching point, they show low resistance and become electrically conductive [1, 2].

For this reason, varistors are used as surge protection devices in a variety of applications, ranging from phone circuitry to high-voltage transformators. In these circuits, varistors are connected in parallel as passive components. When a surge occurs, the varistor becomes conductive and drains the overvoltage from the system [3].

The nonlinear switching characteristic of varistor ceramics is due to a grain boundary effect. As a result of dopants such as Bi_2O_3 segregating to the grain boundary, electrostatic barriers (Double Schottky Barriers (DSBs)) are built up due to the dopants stabilizing acceptor-like defects. These barriers cause the high resistance at low voltages. At a certain voltage, also known as the switching voltage, electrons possess enough energy to cross the DSB, leading to an ion-cascade effect reducing the height of the barrier and thus accelerating current flow through the grain boundary and sample. After the surge is drained, the varistor returns to its initial state [1].

As components are designed to become smaller, the significance of single grain boundaries increases. The electrical characteristics of a small number, or in the extreme case, of one single grain boundary, dominate the behaviour of the whole varistor component [4]. This requires knowledge about single grain boundaries and a detailed characterization process to optimize the electrical properties of components.

Currently, the chemical composition of grain boundaries has only been investigated at μm-level [3]. At the atomic scale, local grain boundary structures and segregation have been studied with transmission electron microscopy (TEM) [5]. However, both studies have used bicrystals instead of commercial multilayer varistor (MLV) material. Outstanding questions,

for example whether the chemical composition of the grain boundary influences electrical behaviour, remain unanswered.

In this thesis, after a short introduction of the underlying material, the electrical characteristics of varistor grain boundaries and fundamentals of the adopted experimental approach (chapter 2), a method for the characterization of single varistor grain boundaries is proposed. This method, described in chapter 3, encompasses electrical as well as chemical characteristics of grain boundaries, with the goal of correlating the electrical characteristics to grain boundary misorientation and to the chemical composition of the sample. A detailed guide is given for the preparation of atom probe tomography (APT) samples using a lift-out technique, and parameters used for the measurement are discussed.

In chapter 4, electrical measurements of single grain boundaries are discussed and categorized. Additionally, APT results of measurements of the bulk varistor material are presented. Ultimately, a complete characterization of two different grain boundaries is presented, complete with a chemical analysis and grain boundary concentration profiles.

Chapter 2

Theory

2.1 ZnO Varistors

The following section outlines the most important physical and chemical characteristics of the investigated ceramic material in this thesis, zinc oxide. Firstly, the crystal structure, physical characteristics and polarity of ZnO are discussed, which is followed by an overview of the manufacturing process of multilayer varistors. Lastly, double Schottky barriers and I-U characteristics are described.

2.1.1 Crystal Structure, Physical Characteristics and Polarity

ZnO occurs in three different crystal structures: the wurtzite (B4-type) structure, zinc blende (B3-type) and the sodium chloride (B1-type) structure. At room temperature, only the hexagonal wurtzite structure is stable [6]. This structure consists of alternating Zn and O layers, with the hexagonally closest packed (hcp) sublayers having half of the tetrahedral interstitial sites occupied by the respective other atom. The wurtzite ZnO structure including the direction of the c-axis can be seen in Figure 2.1 [7].

The space group of ZnO is $P6_3mc$, while the point group is 6mm. Since the geometry, respectively the c/a ratio, of the ZnO unit cell (a = 3.2496 Å, and c = 5.042 Å) is smaller than that of an ideal wurtzite unit cell, the centers of positive and negative charges do not align. Thus, a spontaneous polarisation parallel to the [1000]-direction and inverse to the c-axis is achieved. As there is no inversion symmetry, ZnO is piezoelectric [6].

Due to the missing inversion symmetry, the positive and negative [0001]-direction are not equivalent. The 0001 planes, which are perpendicular to that direction, consist only of zinc or oxygen atoms. Dependent on the crystal orientation, the surface is either terminated by zinc ((0001) plane, "Tail" of polarisation vector) or oxygen ($(000\bar{1})$ plane, "Head" of polarisation vector) atoms. All other planes are non-polar. The polarity leads to varying

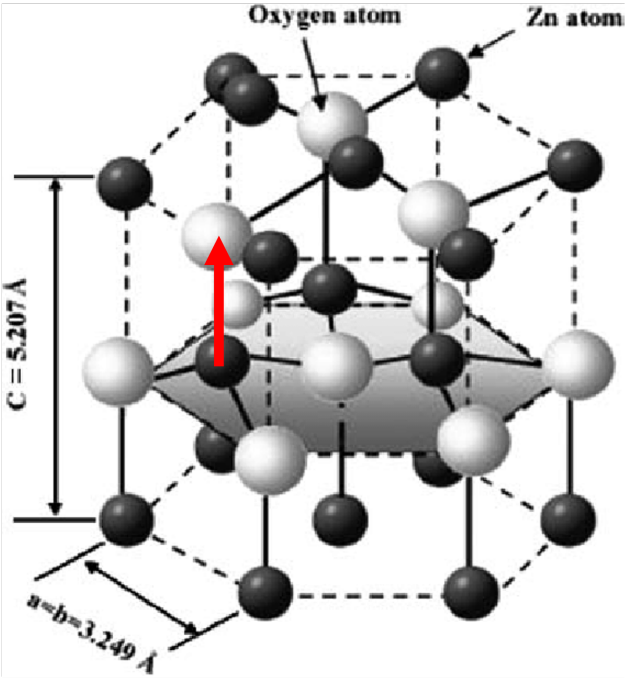

Figure 2.1: the ZnO hexagonal wurtzite structure model, where the tetrahedral Zn-O coordination is shown. Zn is represented by the smaller black spheres, while O is shown by the larger white spheres. The direction of the c-axis is indicated with a red arrow. Adapted from [7].

physical and chemical characteristics of different planes [8].

ZnO is an n-type semiconductor with a band gap of 3.1-3.3 eV, which for commercial use is doped with so-called shallow donors such as Al_2O_3, which is added to increase grain conductivity [9].

2.1.2 Processing Route

Multilayer varistors are manufactured using a homogeneous suspension of ZnO-powder, dopants and organic additives. The processing route is shown in Figure 2.2. The suspension is tapecasted and the electrodes are printed upon the sheets using a mask. The sheets are stacked, laminated and pressed according to the electrode design. After burning out of the binder material, they are sintered and cut out. For cleaning and exposure of the inner electrodes the components are tumbled, after which the front surfaces are capped with liquid metal and the glass layer and the metallisation are burned in. Next, the caps are galvanised using nickel or tin metal spheres in an electrolyte solution. After testing, the finished components are taped onto the circuit boards [10].

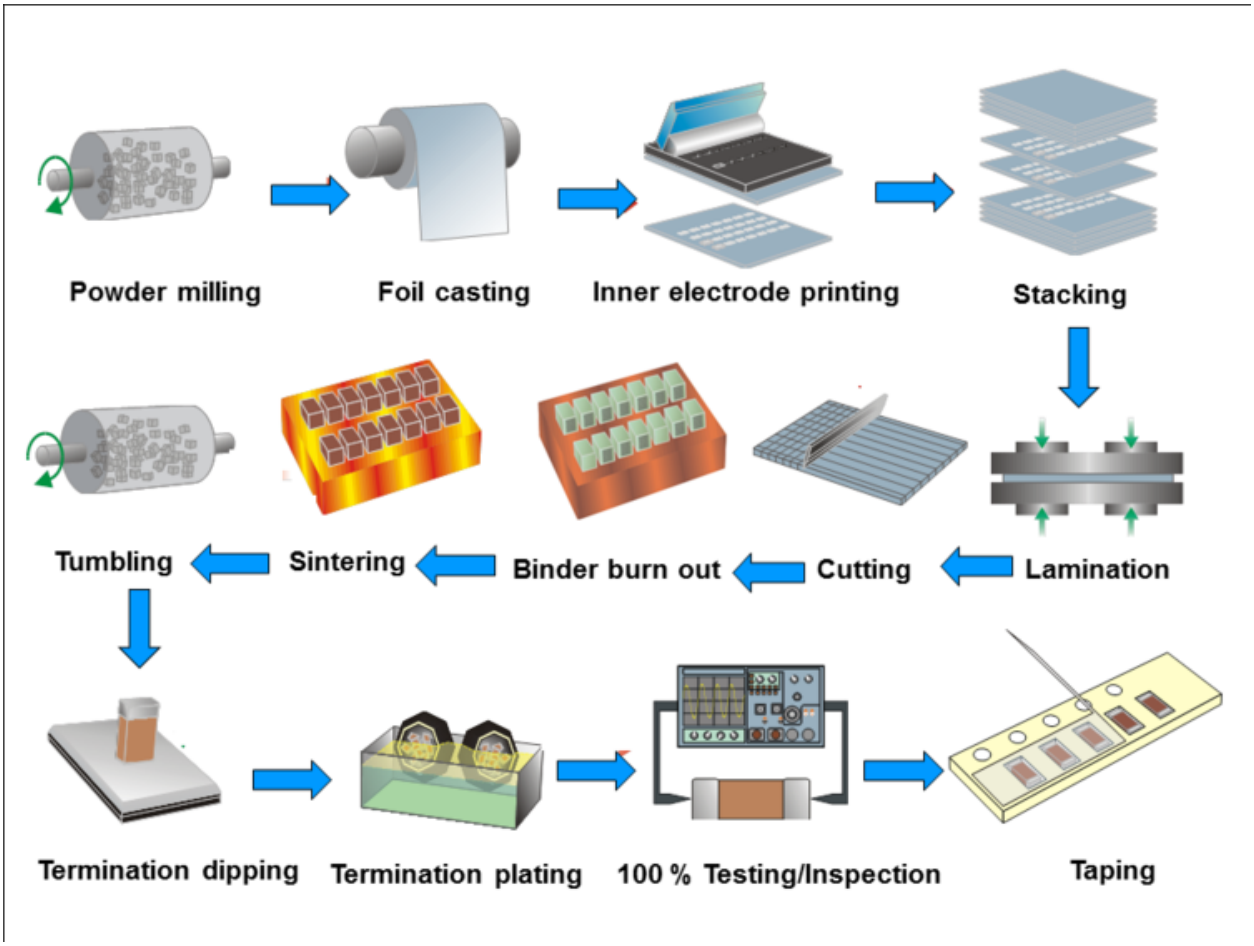

Figure 2.2: the manufacturing process for multilayer varistors, which is similar to that of ceramic capacitors. Adapted from [10].

2.1.3 Double Schottky Barrier and I-V Characteristics

Not only Al_2O_3 is used as a dopant. Additionally, other dopants such as Pr_2O_3 or Bi_2O_3 are added, which create low-melting eutectica. This liquid phase solves the other dopants, which leads to a homogeneous distribution of dopants during sintering. Dopants such as Mn, Co and Al are introduced into the ZnO-lattice, where they act as donors. Other, bigger dopants are present as precipitates, since they cannot be introduced into the lattice because of their size [11]. The grain-boundary material thus contains more defects and dopants, which results in electronic states and a different Fermi level. This leads to a layer of positively charged donor sites on the edges of the grain boundary, as electrons move to the grain boundary to reach thermodynamic equilibrium [12, 13]. This depletion zone is about a 100 nm thick [11]. This leads to a distortion of the valence and conduction band. The potential barrier at a grain boundary is called Double-Schottky barrier (DSB) and is shown in Figure 2.3.

The nonlinear I-V characteristic of a varistor is caused by Double-Schottky barriers at grain

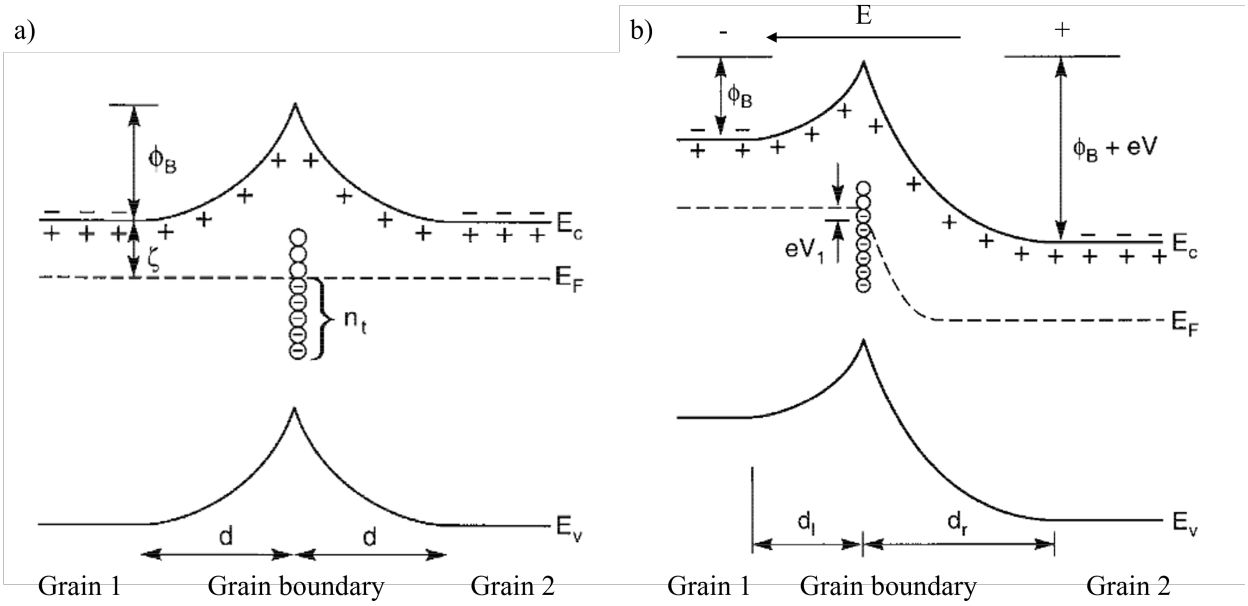

E_V … valence band minimum
E_F … Fermi level
E_C … conduction band minimum

ϕ_B … barrier height
V … applied voltage

Figure 2.3: formation of a potential barrier at a grain boundary, known as a Schottky barrier. Subfigure a) shows the potential barrier without an applied electric field, while Subfigure b) shows the potential barrier with an applied electrical field. Adapted from [1].

boundaries of multigrain varistor materials. In the normal regime, the varistor has a high resistance and only passes a leakage current. However, when the voltage is increased above a certain breakdown voltage, the resistivity changes. As electrons are accelerated by the applied voltage, they become able to cross the DSB and through impact ionisation generate more electron-hole pairs. The electron is raised into the conduction band as the hole recombines at the negative interface, leading to a reduction of the potential barrier [14]. This self-reinforcing reduction of the DSB results in greatly increased conductivity and an increased gradient in the I-V characteristic, as shown in Figure 2.4. In this switching region, there is a power law relationship between the current I and the voltage V, with a non-linearity coefficient alpha. After the potential barrier is removed, the varistor enters a region of high conductivity, which is limited by the bulk conductivity of the ZnO grains. The degradation of the potential barriers is reversible, and after the removal of the high voltage the varistor returns to its previous high-ohmic state [1].

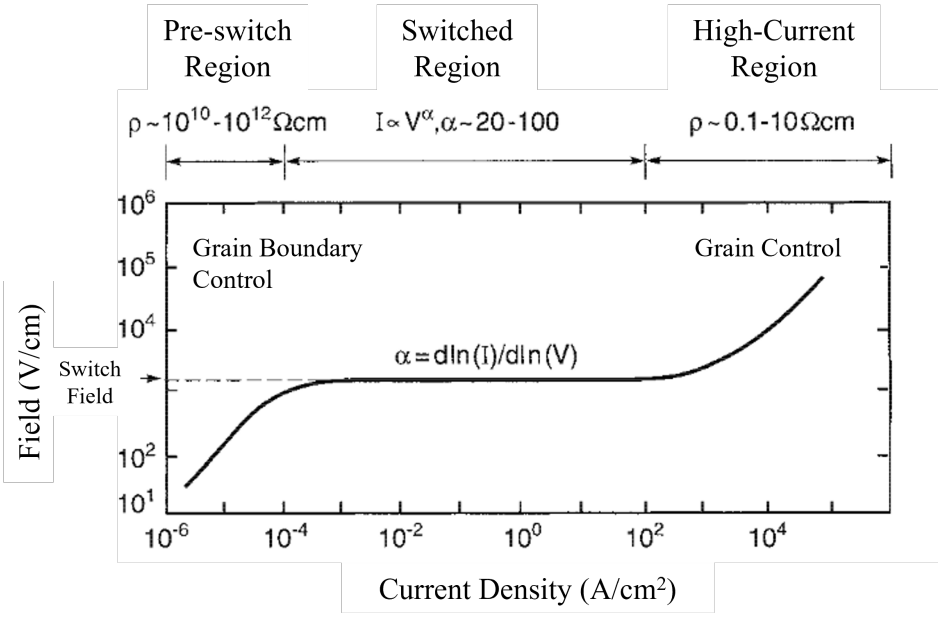

Figure 2.4: Electric field / current density response of a ZnO-based varistor ceramic. As the applied electric field exceeds the switch field, the resistivity of the varistor apruptly decreases, which allows conduction of very large current densities. This process has a switching in the nanosecond range. Adapted from [1].

2.1.4 Grain Orientation and Asymmetry of Double Schottky Barrier

Zinc oxide ceramics exhibit a pronounced piezoelectric effect, where electrical charges are created in response to mechanical stress [15]. This mechanical influence on the electrical properties is known as the piezotronic effect [16].

During the sintering process, due to the the anisotropic thermal expansion of zinc oxide, residual mechanical stresses are introduced into the material as it is cooling [4]. Since the base material is a polycrystalline zinc oxide varistor ceramic with various grain orientations, different grain boundaries have different misorientation angles. This affects their electrical behaviour in the I-V measurement and leads to asymmetry in the DSB, as the piezotronic effect depends on the grain boundary misorientation [17]. The asymmetry is only observed in grain boundaries that have at least one polar axis facing the grain boundary, since the residual stresses due to cooling introduce polar charges at the grain boundary that modify the DSB. This asymmetry is expressed in the I-V measurement through different switching points for each measuring direction, i.e. forwards or reverse. Graphically, the forward and reverse I-V characteristics show a discrepancy and do not align [4].

In this work, the measured grain boundaries are assigned to three ideal archetypes, as seen in [4]. The three archetype are classified as follows:

1. Archetype (mantle-to-mantle): The polar axes of both grains are orientated parallel to

the grain boundary. For this archetype, no asymmetrical DSB and I-V characteristic is expected.

2. Archetype (tail/head-to-mantle): The polar axis of one grain is orientated parallel to the grain boundary, the other perpendicular to the grain boundary. Additionally, the polar c-axis of the perpendicular grain faces away (tail-to-mantle) from or towards (head-to-mantle) the grain boundary. For this archetype, an asymmetrical DSB and I-V characteristic is expected.

3. Archetype (tail/head-to-tail/head): The polar axes of both grains are orientated perpendicular to the grain boundary and the polar c-axes of both grains face either away from or towards the grain boundary (tail-to-tail, head-to-tail or head-to-head arrangement). Depending on the termination at the grain boundary, an (a)symmetrical DSB and I-V characteristic is expected: Head-to-tail grain boundaries have different terminations, thus, an asymmetrical DSB and I-V characteristic is expected. Contrary, head-to-head and tail-to-tail grain boundaries have the same termination at the grain boundary, so no asymmetrical DSB and I-V characteristic is expected.

These archetypes are shown in Figure 2.5. For archetypes 2 and 3, the direction of the polar c-axis perpendicular to the grain boundary can be determined if twin boundaries are identified in a SEM picture, as the polar c-axis is orientated towards the twin boundary [18].

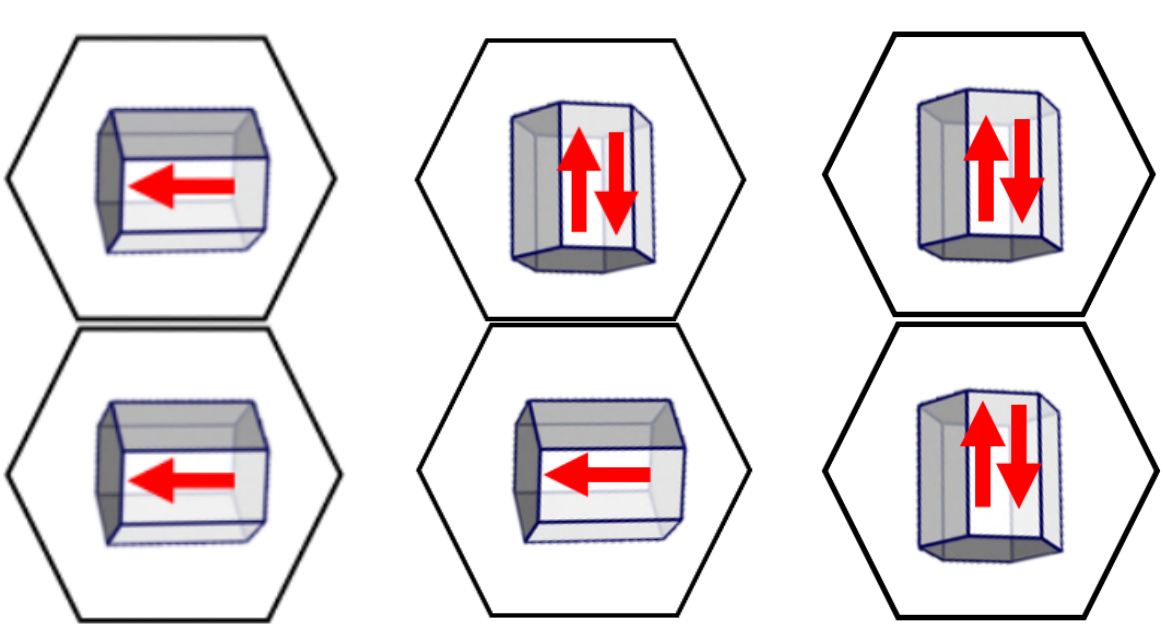

(a) Archetype 1 (b) Archetype 2 (c) Archetype 3

Figure 2.5: An illustration of the three different archetypes. The polar vectors and their directions are shown by red arrows.

2.2 Fundamentals of the Adopted Experimental Approach

In this section, the used experimental techniques are described, starting with focused ion beam and electron backscatter diffraction, followed by atom probe tomography.

2.2.1 Focused Ion Beam (FIB) and Electron Backscatter Diffraction (EBSD)

The *Versa 3D Dual Beam High Vacuum* system from *Thermofischer*, seen in Figure 2.6, was used for sample preparation. The dual-beam system is comprised of a high-resolution scanning electron microscope (SEM) column for imaging and a focused ion beam (FIB) for sample cutting and cleaning using gallium (Ga) ions. The microscope also includes a gas injection system (GIS), which can be used in combination with the ion or electron source to deposit platinum (Pt) ions onto the sample surface. For imaging, the backscatter electron (BSE) and the secondary electron (SE) detector were used. Furthermore, the system is equipped with a micromanipulator (*Omniprobe*^{TM}), which can be used for lift-out of specific micro-features of the sample [19, 20].

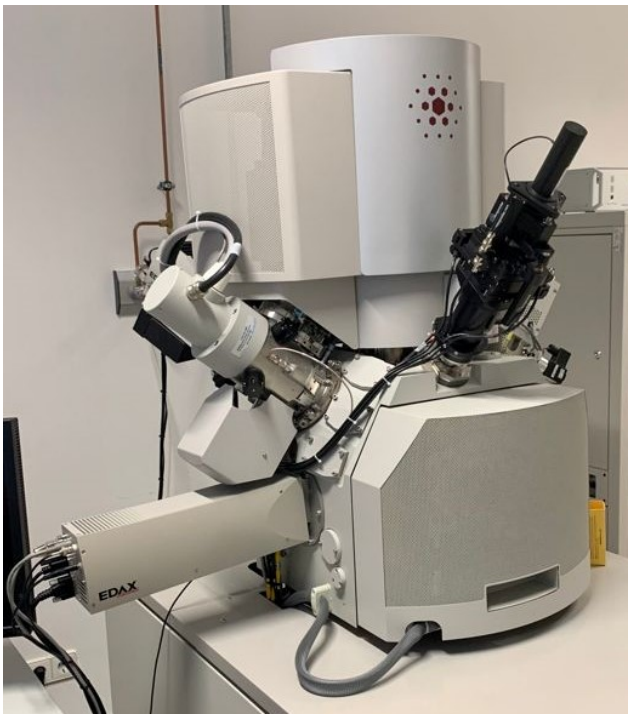

Figure 2.6: The *Versa 3D Dual Beam High Vacuum* system from *Thermofischer*.

To determine crystallographic orientations, an electron backscatter detector (EBSD) was used. For this, electrons from the SEM column are diffracted on the tilted sample. These so-called Kikuchi diffraction patterns are analysed and integrated using an algorithm, the Hough transformation. Thus, the microstructural orientations of grains in the sample can

be acquired. Once orientations of different grains are obtained, the crystallographic misfit between two grains can be determined. This misfit is quantified through the misorientation angle. This describes an axis-angle pair where one crystallographic grain lattice must be rotated upon the given axis by the given angle to obtain the orientation of the second grain [21]. The EBSD analysis in this thesis always uses the c-axis in misorientation angle measurements. The Orientation Imaging Microscopy (OIM^{TM}) Analysis software by *EDAX* was used for evaluation.

The misorientation angle in the tip is measured using transmission-EBSD (t-EBSD), alternatively called Transmission Kikuchi Diffraction (TKD). For t-EBSD analysis, the sample must be electron-transparent, having a thickness of 100 nm or lower. Otherwise, the electrons are not able to pass through the specimen. With t-EBSD, only the last 20 nm of the surface before the electrons exit the sample are imaged to obtain diffraction patterns and thus orientation information [22]. This leads to a higher resolution than conventional EBSD, allowing imaging of features such as grain boundaries in annular-milled specimen tips [23]. Both the misorientation angles in the bulk material and the atom probe tip are measured. If both misorientation angle measurements align, the sample can be measured in the APT. Thus, it is possible to correlate information on the orientation and chemical composition of a defined grain boundary.

2.2.2 Atom Probe Tomography

For the atom probe measurements, a local electrode atom probe (*LEAP 3000 X HR* in laser mode) was used, which can be seen in Figure 2.7. Using this technique, spatial distributions of atomic species can be mapped out in three dimensions (3D), achieving near-atomic resolution [24].

The atom probe is comprised of a high vacuum chamber, a local electrode, a time-resolved position-sensitive detector, a high-voltage source and a laser. In this work, the laser mode of imaging was employed, a technique commonly used for non-conducting materials. In laser mode, a laser pulse over a standing voltage is used instead of a high voltage pulse to excite the sample. The electric field F acting on the tip is given by Equation 2.1:

$$F = \frac{V}{k_f * R} \tag{2.1}$$

V is the applied positive high voltage, k_f is the field factor (usually in the range of 2-10) and R is the radius of the tip, which should be smaller than 100 nm. The smaller the tip radius, the lower the applied electrical field has to be to evaporate ions towards the detector. As it is evaporated, the radius of the sample tip increases. This, according to Equation 2.1, necessitates an increase in the standing voltage. Since there is a maximum standing voltage,

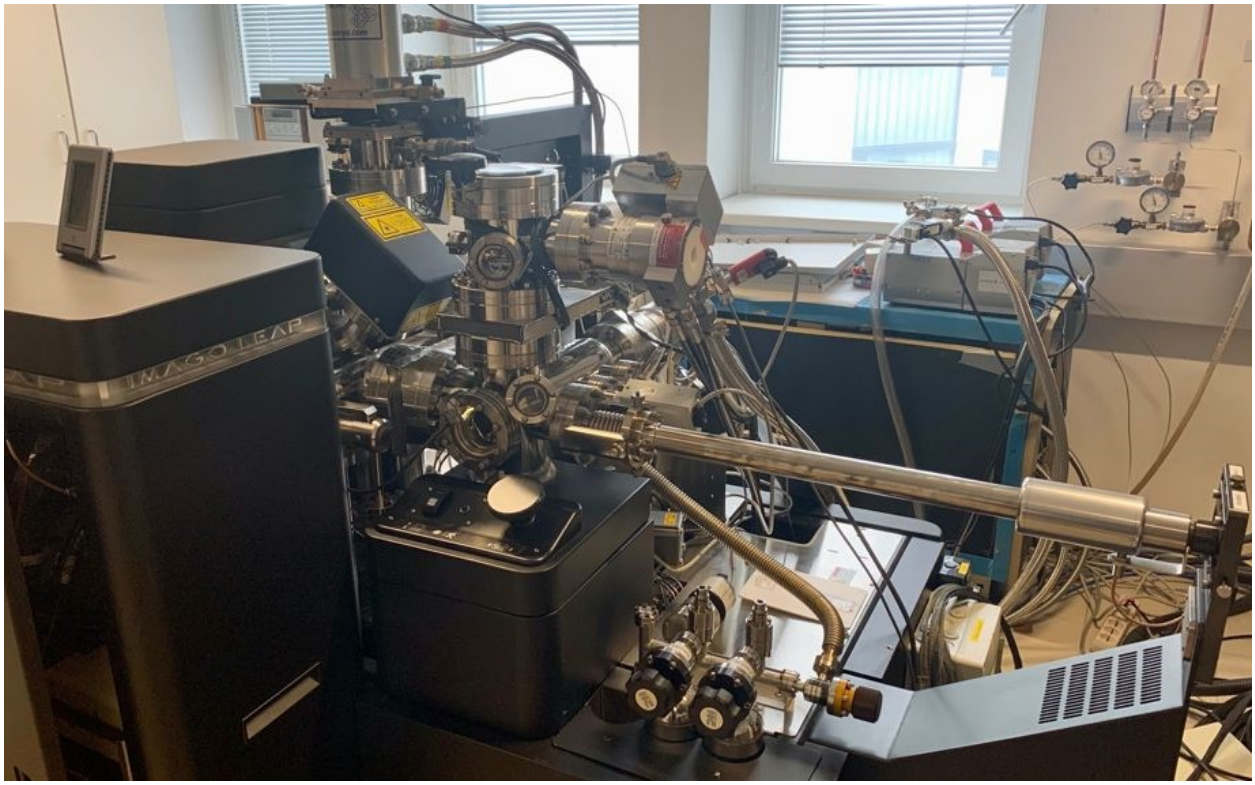

Figure 2.7: The imago LEAP 3000 X HR system.

the measurement has to be stopped after a certain time. This is the reason why a low shank angle in the sample tip is preferred.

The laser pulse prompts the evaporation of ions, which are then accelerated towards the detector. Using the x and y position on the detector, the x and y positions on the sample can be determined. The z position is found by the temporal order of atoms arriving. To avoid the overlap of two almost simultaneously arriving ions, the detector has to have a time separation of a few nanoseconds. The type of ion is determined by measuring the time of flight t, which gives the mass-to-charge ratio M/n of the evaporated ions. This can then be combined with the kinetic energy, leading to Equation 2.2:

$$neV = \frac{1}{2}Mv^2 \tag{2.2}$$

V is the voltage applied, M is the mass of atoms, and v is the velocity of the ions, given by L/t, where L is the flight distance travelled [25]. The experimental setup is shown in Figure 2.8.

Using this data, a mass spectrum can be built up, which can then be combined with the spatial data to generate a 3D reconstruction, which is usually within the first 100 nm of the sample tip. An example of such a mass spectrum is shown in Figure 2.9.

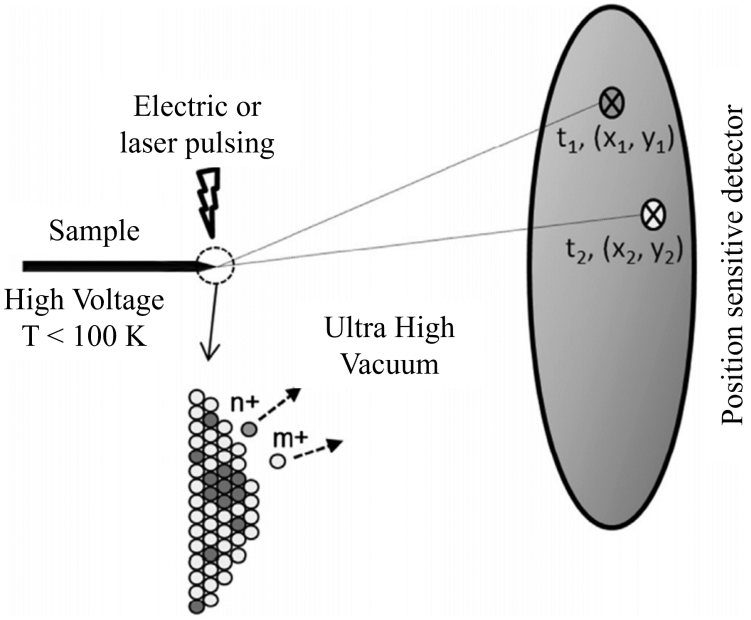

Figure 2.8: A schematic of the experimental setup used in atom probe tomography. Adapted from [25].

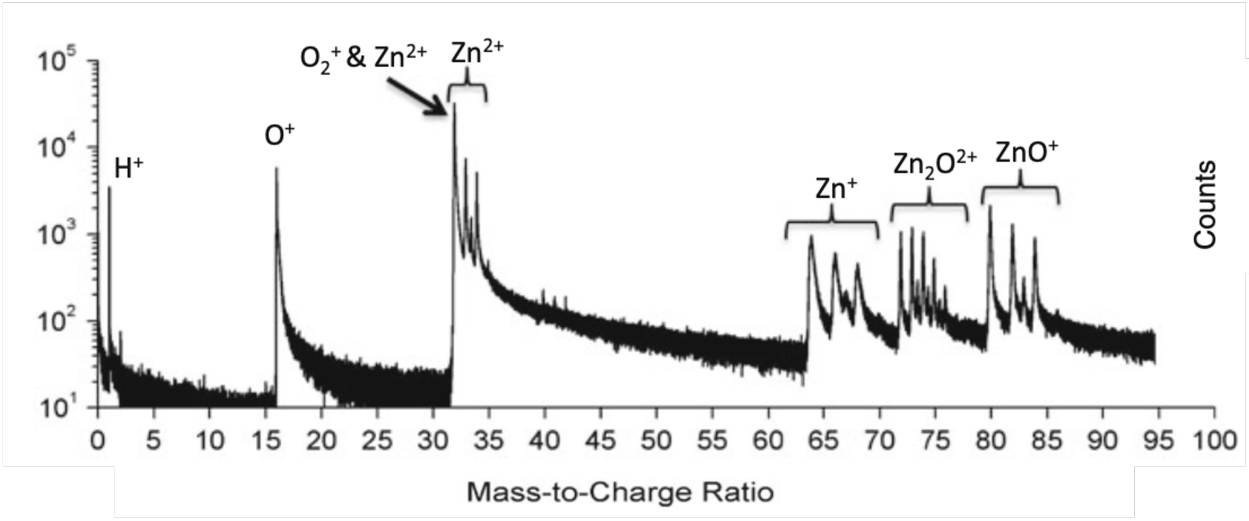

Figure 2.9: An example mass-to-charge ratio spectrum of a Zinc Oxide Nanowire grown using O_2/Ar measured in pulse laser mode. The x axis denotes mass-to-charge ratio, while the y axis denotes counted ions. The O_2^+ and the $^{64}Zn^{2+}$ peak coincide. Adapted from [26].

Chapter 3

Material and Methods

In this chapter, the sample material is described, continued by an introduction to the 4-pole electrical measurement technique. In the next section, EBSD and the lift-out method are detailed, followed by a description of the APT measurements and relevant parameters.

3.1 Material and Powder Composition

The sample material was provided by EPCOS OHG, a TDK group company. Two different specimen types were examined in this thesis. The first are multilayer varistors (MLVs) with internal electrodes, the second are pre-cut specimens of bulk energy varistors, designated as energy varistors (EVs). Both sample types have a similar initial powder composition (bismuth-based ZnO), given in for the EV samples in Table 3.2, but due to the different design of the sample types they are manufactured differently. While the bulk energy varistors underwent a sintering (maximum temperature 1180 °C) and tempering process (burning-in process of glassy layer, maximum temperature 540 °C), the MLVs have to be sintered at a lower temperature due to co-sintering with metal electrodes. This results in different average grain sizes.

MLV specimens are of multilayer varistor material interdispersed with inner palladium (Pd) electrodes and capped with silver. This sample type has an average grain size of 5 - 15 μm (MLVs). This type of varistor was manufactured commercially for experimental purposes. An example of an MLV, both polished and unpolished, and its microstructure is presented in Figure 3.1. For better legibility the specimen designation is reduced to MLV#No., where No. refers to the specimen number.

EV specimens are cut from commercial energy varistors, shown in Figure 3.2(a) and 3.2(b). Figure 3.2 shows an energy varistor cylinder, a sample marked for cutting and a SEM picture of the polished specimen structure including different grains. This sample type has an average grain size of 10 - 30 μm. EV specimens are designated V6T1#No., where V stands for

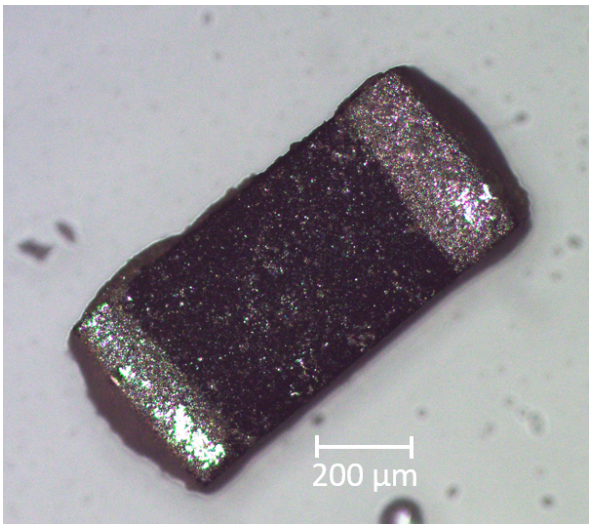

(a) unpolished MLV

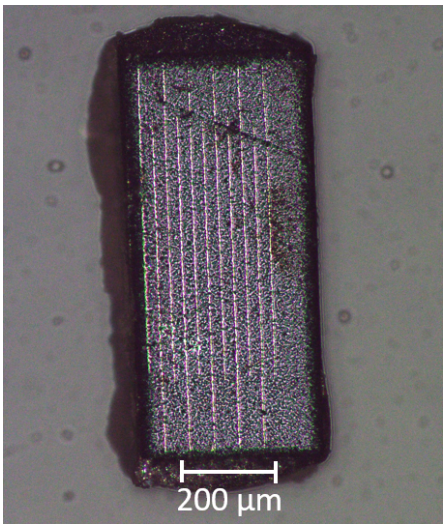

(b) polished MLV

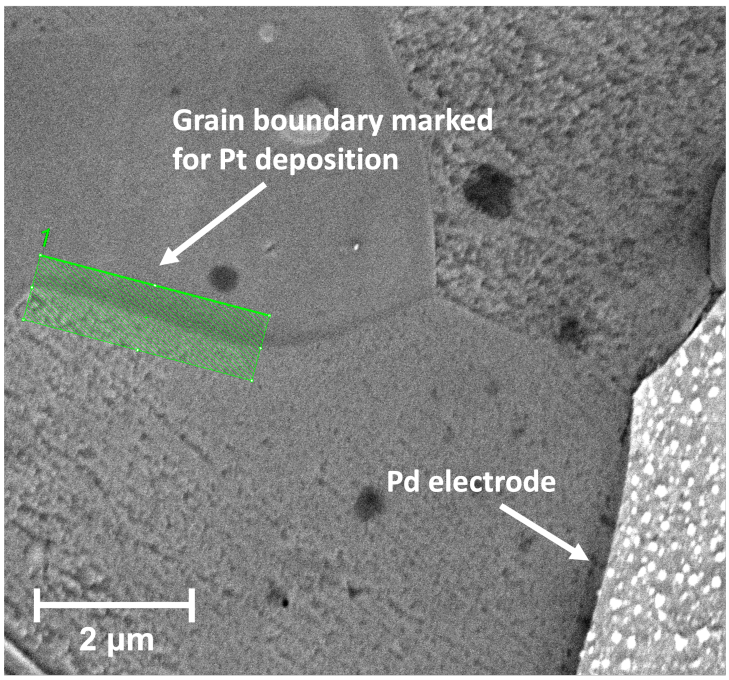

(c) microstructure of MLV

Figure 3.1: Image of MLV in the unpolished (a) and polished (b) state taken with a digital light microscope. C) shows a SEM image of the MLV microstructure. In b), the palladium electrodes can be seen clearly. One palladium electrode can also be made out in the right-hand corner in c).

varistor and 6 indicates the composition. T refers to the tempering profile, with 1 indicating a standard tempering. No. stands for the number of the specimen. A summary of all investigated samples and the performed measurements is given in Table 3.1.

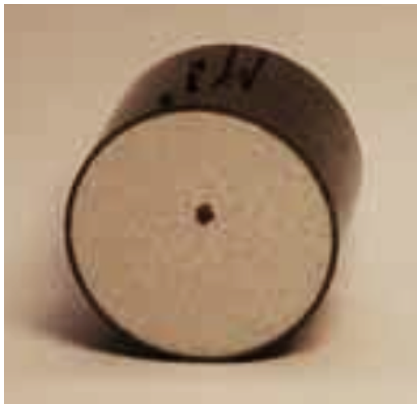

(a) Bulk energy varistor cylinder with a diameter of 40 mm.

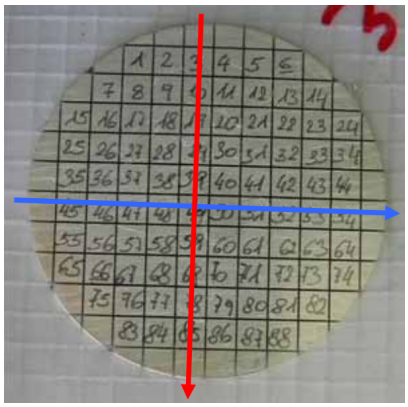

(b) EV material marked for cutting into smaller samples. The red and blue arrows indicate axis directions for counting the specimens.

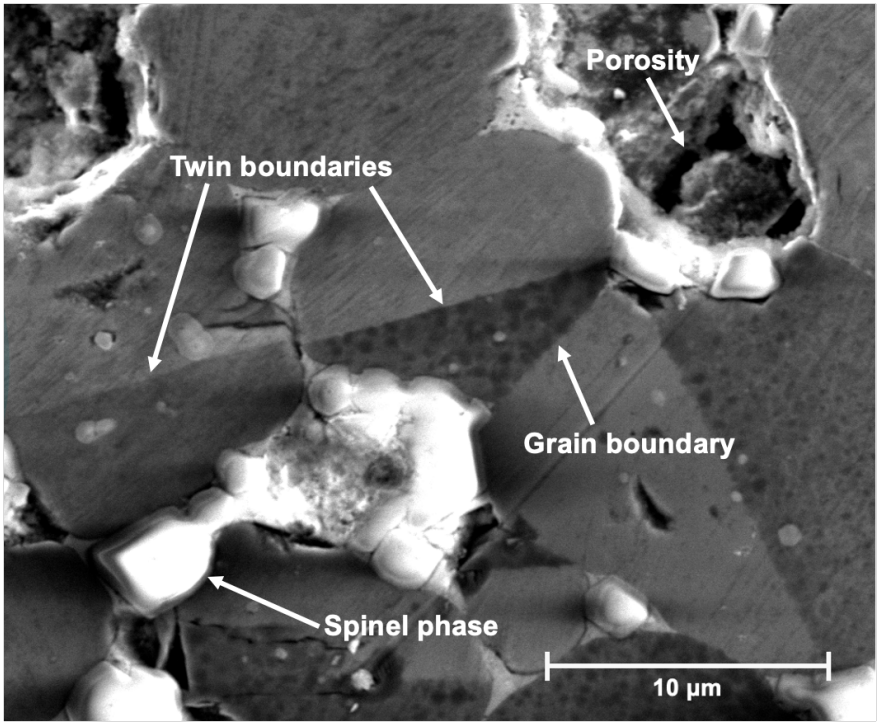

(c) SEM image of EV material etched with oxide dispersion solution (OPS). Grain and twin boundaries as well as spinel phase can be seen.

Figure 3.2: EV specimens: Energy varistor cylinder, both whole (a)) and partly cut and marked (b)). C) shows a SEM image taken of the EV microstructure. Both a) and b) are adapted from [27].

The composition of the powder preparation used for the samples investigated in this thesis is

Table 3.1: Summary of investigated samples, their designation and performed measurements.

Type	Designation	Performed Measurements
MLV	MLV#34	PS4 electrical, APT bulk and grain boundary measurements
EV	V6T1#76	PS4 electrical and APT bulk measurements
EV	V6T1#83	PS4 electrical and APT grain boundary measurements

given in Table 3.2. For each constituent, the share of the cations in the chemical formula is given in atomic percent, with all cation components totalling 100%. Only for the the silver glass frit the share is given in weight percent. The total oxygen percentage can be calculated from adding the amount of oxygen from the chemical formulas and dividing this amount by the total percentage added to the total oxygen percentage.

Table 3.2: Nominal composition of powder preparation used for manufacturing EV samples investigated in this thesis. The deviation from 100 at.% in the Total sum is due to rounding errors. Adapted from [27].

Raw Material	Chemical Formula	Element of Interest	Composition [at.%]
Zinc Oxide	ZnO	Zn	92.3071
Bismuth Oxide	Bi_2O_3	Bi	1.9452
Cobalt Oxide	Co_3O_4	Co	1.0020
Manganese Oxide	Mn_3O_4	Mn	0.4775
Antimony Oxide	Sb_2O_3	Sb	1.9451
Chromium Oxide	Cr_2O_3	Cr	0.9428
Nickel Oxide	NiO	Ni	0.9878
Silicon Oxide	SiO_2	Si	0.3884
Alumina Nitrate	$Al(NO_3)_3 * 9H_2O$	Al	0.0059
Silver glass frit	$No.531001$	/	0.1 (wt.%)
Total			100.0018

3.2 Sample Preparation

Both the MLV samples and the pre-cut EV samples were prepared for the electrical measurements by grinding and polishing the samples that were previously embedded in epoxy. By employing a series of successively finer abrasives a final grinding particle size of 1 μm was achieved. The samples used for illustration of the microstructure in the SEM, such as 3.2(c), were further polished with oxide dispersion solution (OPS) to guarantee visibility of twins. All other samples were polished with 1 μm abrasive diamond polishing solution, to ensure good quality of the electrical measurements.

3.3 Micro 4-Pole Electrical Measurements

The I-V characteristic was measured using a micro 4-pole method, the Prober Shuttle 4 (PS4), manufactured by Kleindiek Nanotechnik GmbH. This method is used to eliminate the contact resistance between the measuring electrode and the sample material, which can create resistances in the same size range as the measured resistances of the varistor material. A sample setup can be seen in Figure 3.3(a). For the measurement, two tips are positioned in each grain of the grain boundary to be measured. The other tips are used to introduce the current, while the inner tips are used to measure the voltage dip.

The PS4 system consists of four tungsten micromanipulators, which are mounted on a substage. This setup can be seen in Figure 3.3(a). The electrical measurement is conducted using a digital multimeter with a combined DC-source with two measuring channels (Keithley 2634B, Keithley Inc., Cleveland, Ohio, USA). A circuit diagram of the PS4 system, measuring the I-U characteristic of a single grain boundary, is shown in Figure 3.3(b). The two tips that provide the current are connected to a Hi- and a Lo- entrance of one channel each, while the other tip on the same grain is connected to the same entrance (Hi- and Lo-, respectively).

The measuring current is applied voltage-controlled in a range of 0 to 4 V with a maximum current of 10 μm, this amounts to around 150 measuring points. To ensure electrical contact of the tungsten measuring tips to the ZnO grains, the contact voltage is measured. This is done by connecting both tips in a grain to the same channel and applying currents of up to 100 nA. Using the PS4 system, contact voltages of up to 0.6 mV are achievable, this corresponds to a contact resistance in the kΩ range. The measurements were conducted using the TSP express software and later evaluated using a *Mathematica* script.

The first step to selecting grain boundaries is to measure several grain boundaries and record their I-V characteristics. These can then be correlated with the crystallographic mismatch obtained from the EBSD data.

3.4 EBSD and Lift-Out Technique

3.4.1 Selection of Grain Boundaries via EBSD

After the electrical measurement the sample is mounted onto a FIB sample holder and introduced into the microscope. The electrically measured grain boundaries are then measured using EBSD. A sample EBSD scan can be seen in Figure 3.4. The Euler angles and subsequently the mismatch between the two grains is calculated for each grain boundary. For the lift-out and following APT characterization defined grain boundaries were selected. The first group were grain boundaries with close conformity to a mantle-tail configuration. These

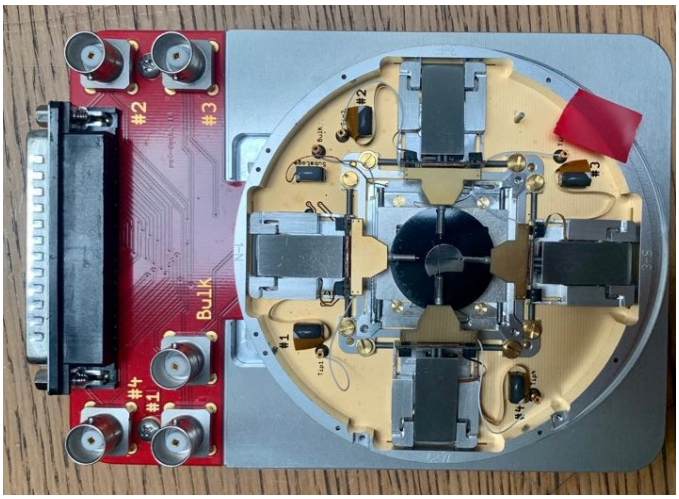

(a) The PS4 system.

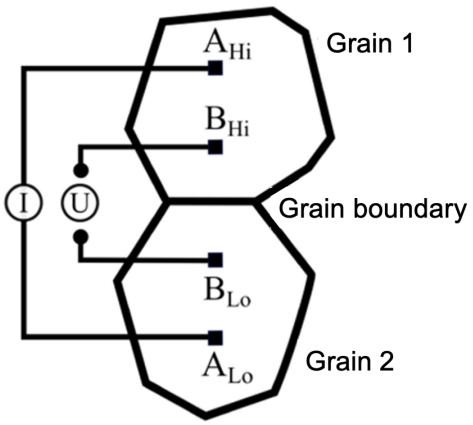

(b) Circuit diagram of experimental set-up. Adapted from [4].

Figure 3.3: PS4 system and corresponding circuit diagram: The tips which provide the current are connected with the Hi- and Lo- entrances of one channel. The tips on the same grain are connected to the respective other channel.

were selected as they have the highest asymmetry in their electrical measurements. The second group were grain boundaries with a symmetrical I-V characteristic, for example grain boundaries with a tail-to-tail configuration. Using this method, the difference in chemical composition of grain boundaries in different configurations can be characterized.

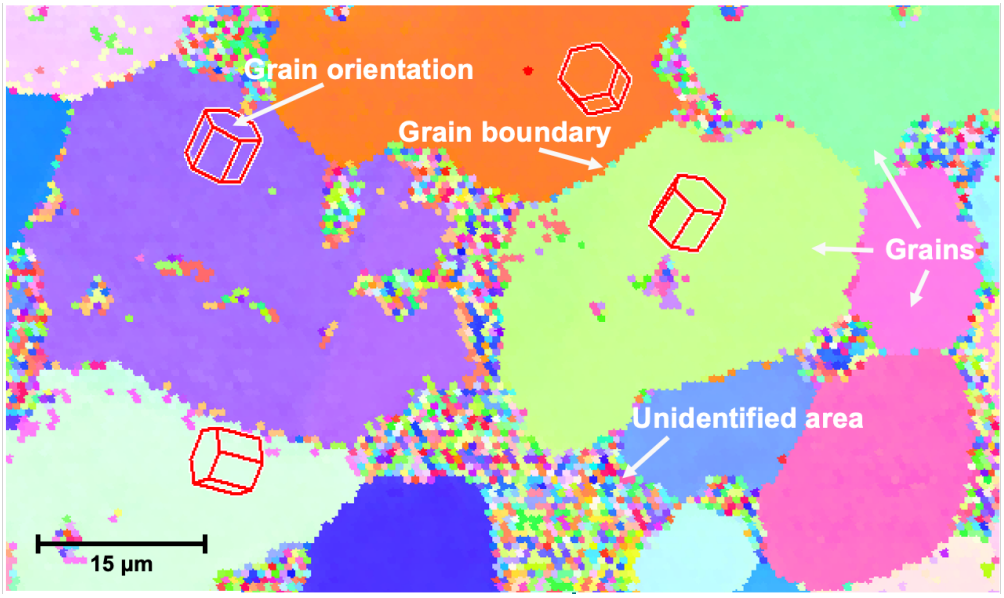

Figure 3.4: EBSD scan of sample type B. The different grains can be clearly seen, as well as areas of non-wurzite crystalline structure (intergranular and spinel phases) and grain boundaries. The red wire-frame hexagonal crystal lattice overlays denoting grain orientation were added using the *OIM Analysis* software.

3.4.2 Lift-Out and Tip Preparation for Atom Probe Tomography

Using the GIS, the selected grain boundaries are highlighted with a platinum layer, to protect the grain boundary from Ga implantation. Afterwards, the grain is marked with a fine line cut into the platinum layer. They are then cut out on three sides and the underside using the FIB, while the sample is rotated to 52°. An example lift-out can be seen in Figure 3.5.

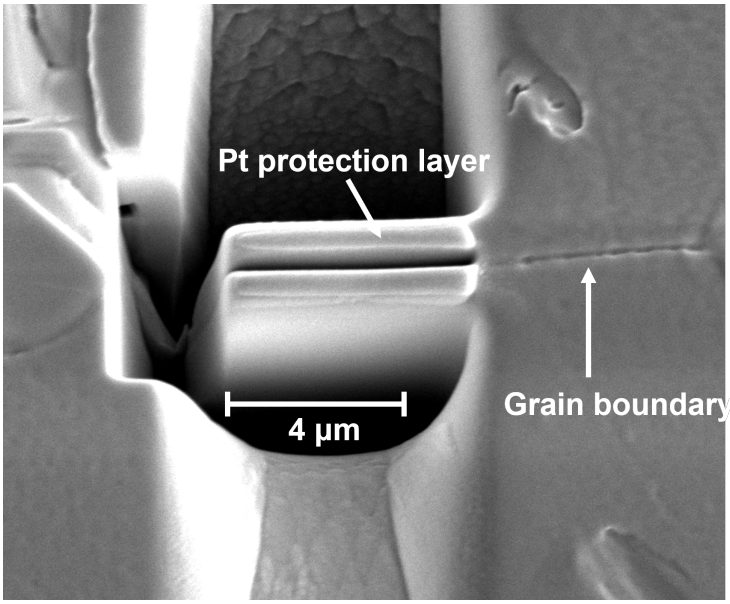

Figure 3.5: A sample lift-out. The grain boundary can be clearly seen and is first protected with a layer of platinum (Pt) deposited by the GIS. This layer is then milled using gallium ions, producing a fine line which denotes the grain boundary position.

Following, the sample is rotated back to zero degrees and both the micromanipulator and the GIS are introduced. The micromanipulator is then affixed to the prepared cantilever using platinum deposition, which is followed by cutting out the cantilever. The Omniprobe and affixed sample are retracted and the sample is replaced in the microscope by an electropolished APT-tip, on which the sample is then fixed using platinum deposition and the GIS.

The sample is then annular milled to achieve the desired geometry for APT measurements. Intermittently, the tip is measured using transmission-EBSD (also known as Transmission Kikuchi Diffraction technique, abbreviated as TKD) to confirm that the desired interface is within 100 nm of the tip, and also to confirm the same crystallographic mismatch of the interfaces as the original grain boundary. Experience has demonstrated that TKD is best done after each milling step, to not lose the grain boundary during a too-long milling. At first, 30 kV and 0.3 nA to 49 pA should be used for the milling, decreasing the current with each milling step. This prevents amorphisation of the sample and also ensures a slow-enough milling speed to allow for monitoring the grain boundary. For the last steps, to achieve the

desired accuracy and also functioning as cleaning, 8 kV and 60 to 30 pA should be used in the FIB. Further information on the used method can be found in [23].

3.4.3 Using Microarrays instead of electropolished Tips

As the electropolished tips were breaking after a certain turn-on-voltage in the atom probe, usually around 3000 kV, another sample preparation method was chosen. Instead of using the pre-polished tips, the lifted-out ZnO material was affixed to a silicon (Si) microarray, containing 36 pre-cut tips. Only the outer tips should be used, as with the inner tips there is shading by the outer tips during the TDK measurement. A scanning electron microscopy (SEM) picture of the Si microarray can be seen in Figure 3.6.

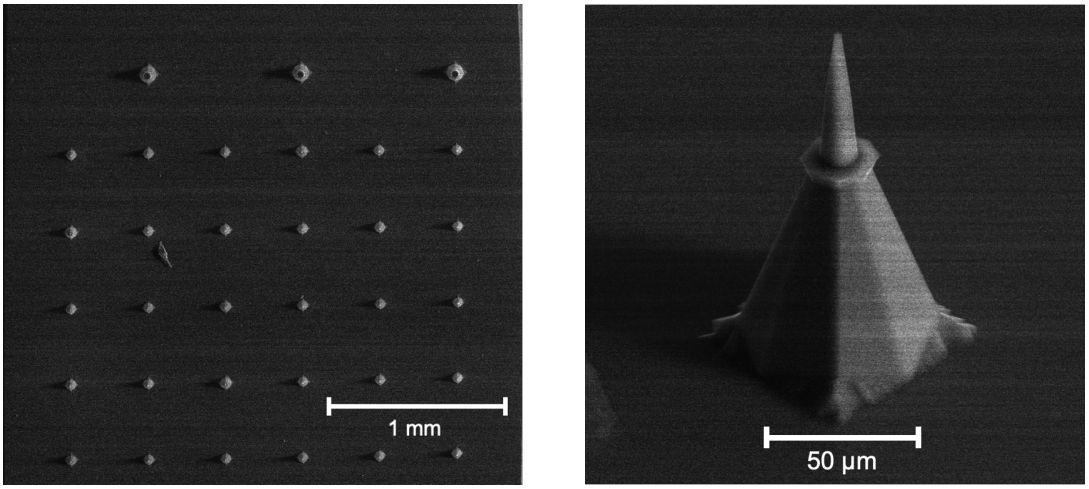

(a) Si microarray, top view (b) Si-microarray, side view

Figure 3.6: SEM pictures (analytical imaging mode) of Si microarray as seen from the top (a) and a single Si pylon seen from the side (b).

This method allowed for easier tip preparation, as the tip is already finished beforehand and the sample only has to be affixed with Pt ions on two sides. However, upon introduction into the atom probe and starting the measurement, the tips immediately break. This is because of the difference in thermal and electrical conductivity between the microarray material (Si) and the sample tip material (ZnO), as heat accumulates on the interface. For this reason, the electropolished tips were used again, this time with more Pt ion-deposition used to stabilise the tip during milling and the measurement.

3.5 APT Measurements

When the tip has been milled to the desired radius and shank angle, it is introduced into the APT measurement chamber. It is important to do this as soon as the annular milling

in the FIB is finished, as there can be degradation of the tip or contamination with dust in a non-vacuum atmosphere. Special care has to be taken to not damage the tip during introduction into the atom probe microscope, as tips can be easily damaged.

Measurements were performed in laser mode at 40 to 60 K, 200 or 250 kHz, 0.2 - 0.6 nJ pulse energy and 0.5% target evaporation. Further information on the variation of measurement parameters can be found in chapter 4.2. For evaluation, the *IVAS 3.6.8* software from *Cameca* was used.

Chapter 4

Results and Discussion

In this chapter, the I-V characteristics of the measured grain boundaries are discussed and classified into symmetrical and asymmetrical measurements. Secondly, the bulk varistor material is investigated in the atom probe microscope and a parameter study is presented. Thirdly, two APT measurements of grain boundaries with distinctly different I-V characteristics are introduced and analysed.

4.1 I-V Characteristics of different Grain Boundaries

In total, 30 grain boundaries were measured using the 4-pole method. Of these, 28 were scanned using EBSD, and 20 I-V characteristics were correlated with their EBSD scans and respective grain boundary misorientation angles. The 12 most representative grain boundaries were classified primarily according to their I-V characteristics (symmetrical or asymmetrical) and secondarily according to their archetypes (see Figure 2.5) and are represented here. Asymmetry generally occurs in the leakage current region. A grain boundary I-V curve measurement was classified as asymmetric if the logarithmic plots of the forward and reverse measurement differ by a factor of 1.7 or more.

If the angle of the c-axis towards the grain boundary was lower than 45°, the grain was classified as a mantle interface. A bad fit to an archetype is indicated when the grains could be sorted into two different archetypes, but favor one more than the other. Generally, most grain boundaries cannot be classified as one distinct archetype, as would be possible when measuring bicrystals. Where no classification was possible, the grain boundary was excluded from the analysis. Additionally, grain boundaries with non-conclusive EBSD scans were also excluded.

4.1.1 Electrical and EBSD Measurements of Grain Boundaries with symmetrical I-V Characteristic

In this section, corresponding I-V curves and EBSD scans of grain boundaries with symmetrical I-V characteristics are presented. After an initial assessment of the EBSD scan and measurement of the misorientation angle, they are classified into the different archetypes presented in section 2.1.4., taking into account whether the grain boundary corresponds well to the archetype or not.

Each pair of subfigures shows an electrical and EBSD measurement of a different grain boundary, of which two or more different measurements were made. Each measurement was conducted in two directions, forward ("fwd") and reverse ("rev"). Generally, measurements from MLV (MLV#34) and EV (V6T1#76 and V6T1#83) specimens were investigated.

In Figure 4.1, different symmetrical I-V characteristics and EBSD scans of grain boundaries (GBs) corresponding to Archetype 1 are shown. All presented measurements appear to be well aligned with archetype 1. This is illustrated by corresponding EBSD pictures and lattice overlays shown in Figures 4.1(b), 4.1(d) and 4.1(f). These grain boundaries are not polar, since the polar axes are parallel to the grain boundary and each other. Thus, no natural asymmetry of the DSB and I-V characteristic is expected, which is confirmed through the experimental data.

In Figure 4.2, different symmetrical I-V characteristics and EBSD scans of grain boundaries corresponding to Archetype 2 are shown. These grain boundaries do not align well with archetype 2. This is corroborated by corresponding EBSD scans, shown in Figures 4.2(b) and 4.2(d). These grain boundaries exhibit less polar interfaces at the grain boundary, since the polar c-axes are tilted away from the grain boundary. Thus, a more symmetrical I-V characteristic is expected and seen in the respective measurements, for example in Figure 4.2(a), where there is no discrepancy between the forwards and reverse directions.

For archetype 3, the polar c-axes facing the interface are both zinc-terminated (tail-to-tail alignment), the I-V characteristic is expected to be symmetrical, as described in [28]. Figure 4.3(a), shows a measurement of a grain boundary with a good fit to this archetype, according to the EBSD scan in Figure 4.3(b).

The results in the preceding section, summarized in Table 4.1, align well with data measured and analysed in [4], where grain boundaries were also measured using the 4-pole method and classified according to their archetype using EBSD. However, since the orientation of the grain below the grain boundary is not known, the influence of grain orientation on the I-V characteristic cannot be fully determined by an electrical measurement and an EBSD scan. Thus it is recommended to determine the grain boundary misorientation and archetype after the electrical measurement and lift-out by cutting and grinding the specimen perpendicularly

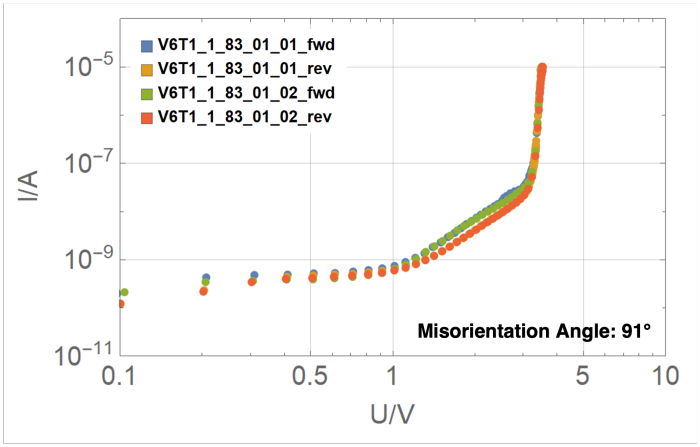

(a) Symmetric I-V characteristic (V6T1#83 GB1).

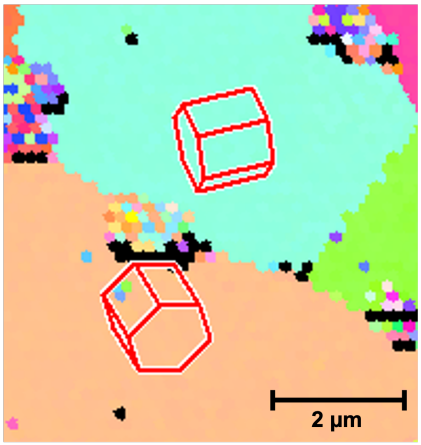

(b) EBSD scan of grain boundary 1.

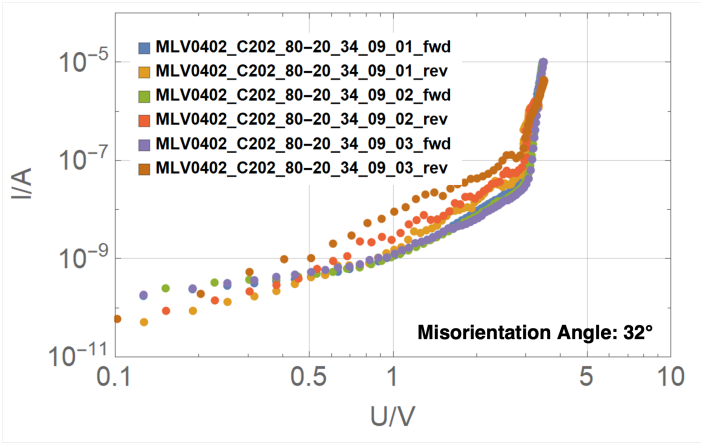

(c) Symmetric I-V characteristic (MLV#34 GB9).

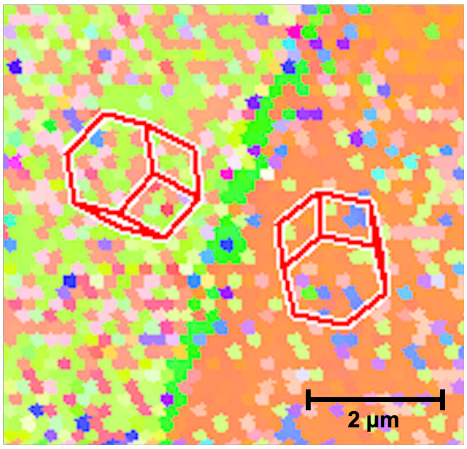

(d) EBSD scan of grain boundary 9.

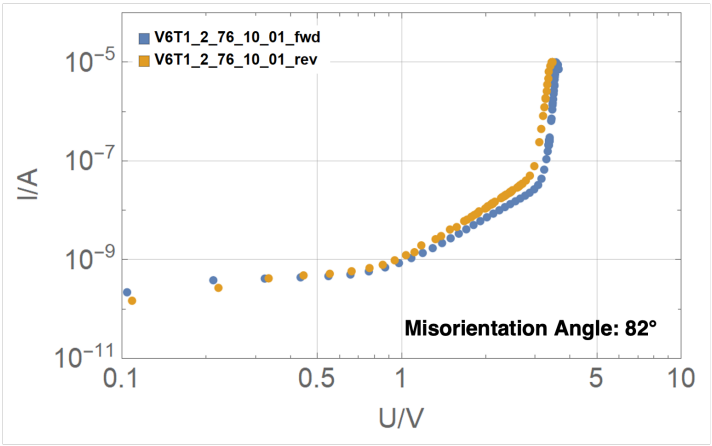

(e) Symmetric I-V characteristic (V6T1#76 GB10).

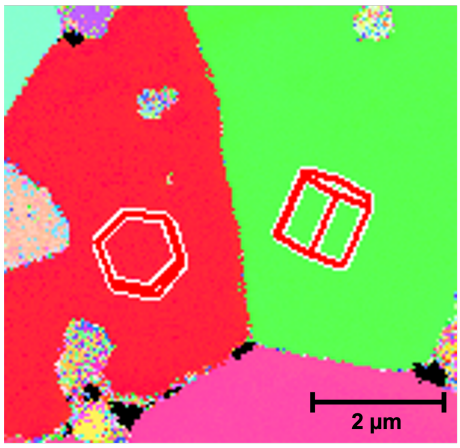

(f) EBSD scan of grain boundary 10.

Figure 4.1: Symmetric I-V characteristics of grain boundaries with EBSD scans corresponding to archetype 1.

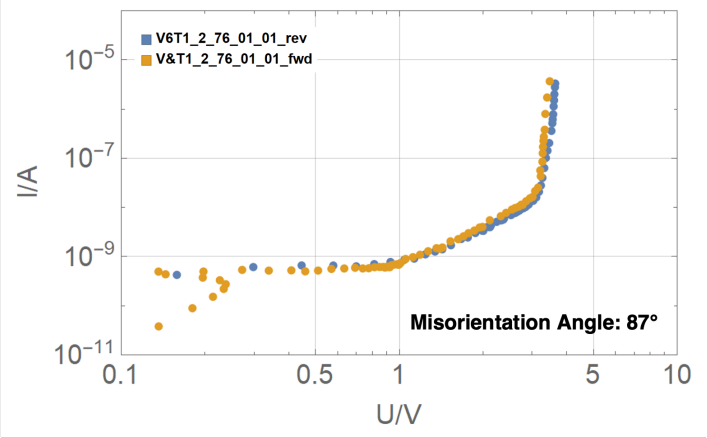

(a) I-V characteristic with misorientation angle of 91°

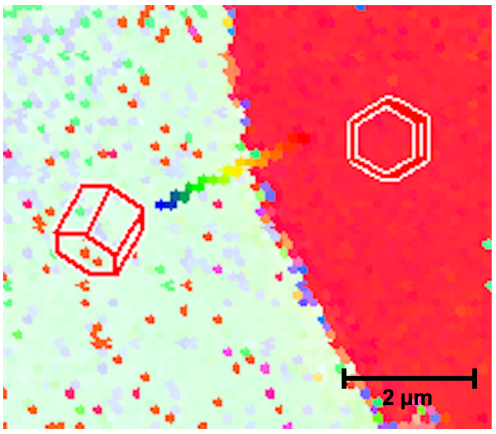

(b) EBSD scan of grain boundary 1.

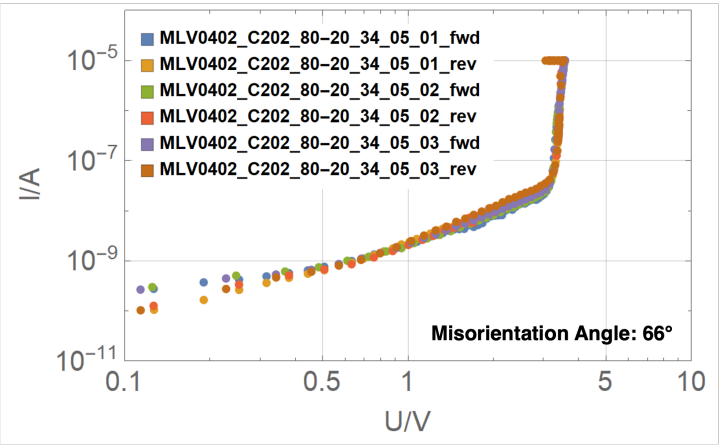

(c) Symmetric I-V characteristic (MLV#34 GB5).

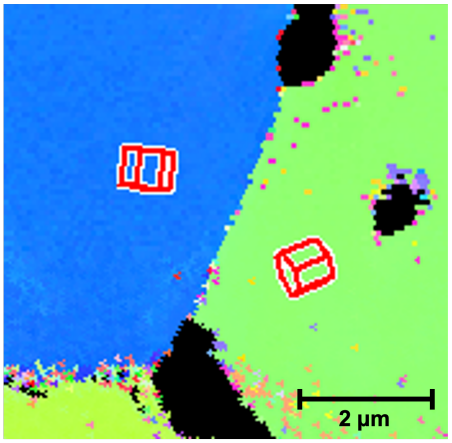

(d) EBSD scan of grain boundary 5.

Figure 4.2: Symmetric I-V characteristics of grain boundaries with EBSD scans corresponding to archetype 2.

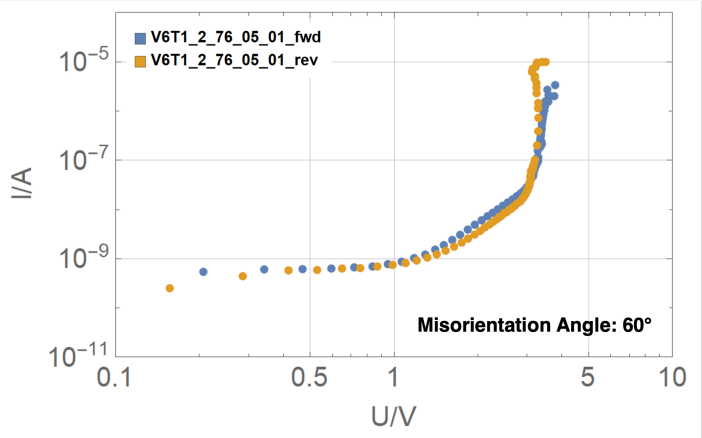

(a) Symmetric I-V characteristic (V6T1#76 GB5).

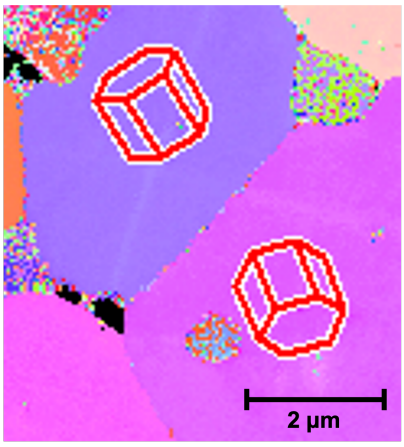

(b) EBSD scan of grain boundary 5.

Figure 4.3: Symmetric I-V characteristic of grain boundary with EBSD scan corresponding to archetype 3.

to the grain boundary. This exposes the microstructure of the measured grain boundary so that a definitive classification can take place.

Table 4.1: Summary of grain boundaries with symmetrical I-V characteristics. The sample and grain boundary (GB) number, proposed archetype and misorientation are given. Additionally, an assessment of alignment with the proposed archetype (either good or bad) is given.

Sample No.	GB No.	Proposed Archetype	Misorientation Angle	Aligment with Archetype
V6T1#83	1	mantle-to-mantle	91°	good
MLV#34	9	mantle-to-mantle	32°	good
V6T1#76	10	mantle-to-mantle	82°	good
V6T1#76	1	mantle-to-tail	87°	bad
MLV#34	5	mantle-to-tail	66°	bad
V6T1#76	5	tail-to-tail	60°	good

4.1.2 Electrical and EBSD Measurements of Grain Boundaries with asymmetrical I-V Characteristic

In this section, corresponding I-V curves and EBSD scans of grain boundaries with asymmetrical I-V characteristics are presented. After an initial assessment of the EBSD scan and measurement of the misorientation angle, they are classified into the different archetypes presented in section 2.1.4., taking into account whether the grain boundary corresponds well to the archetype or not.

Each pair of subfigures shows an electrical and EBSD measurement of a different grain boundary, of which two or more different measurements were made. Each measurement was conducted in two directions, forward ("fwd") and reverse ("rev"). Generally, measurements from MLV (MLV#34) and EV (V6T1#76 and V6T1#83) specimens were investigated.

In Figure 4.4, two different asymmetrical I-V characteristics and EBSD scans of grain boundaries (GBs) corresponding to Archetype 1 are shown. The presented measurements are well aligned with archetype 1. This is illustrated by corresponding EBSD pictures and lattice overlays shown in Figures 4.4(b) and 4.4(d). It should be noted that the I-V measurement in Figure 4.4(a) exhibits significant drift. Since these grain boundaries were classified as mantle-to-mantle interfaces and show good alignment with the archetype, no natural asymmetry of the DSB and I-V characteristic is expected. Nevertheless, the I-V characteristics are still asymmetrical, highlighting the need for further classification of the grain boundary through perpendicular cutting and grinding. This allows for a determination of the orientation below the surface.

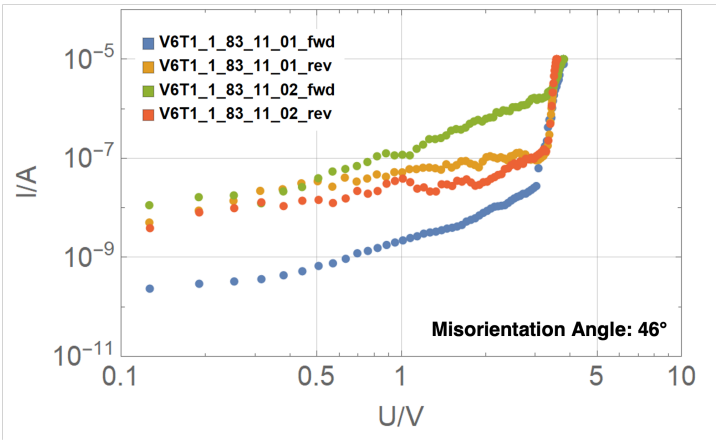

(a) Asymmetric I-V characteristic (V6T1#83 GB11).

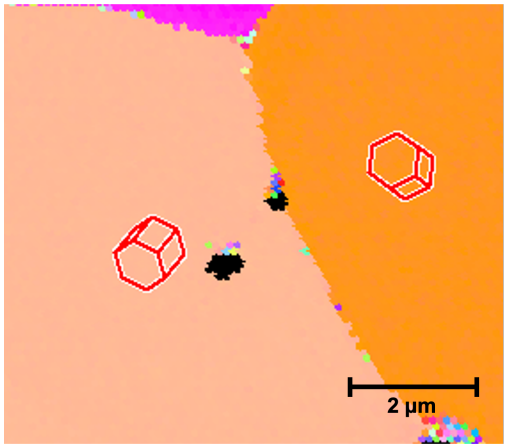

(b) EBSD scan of grain boundary 11.

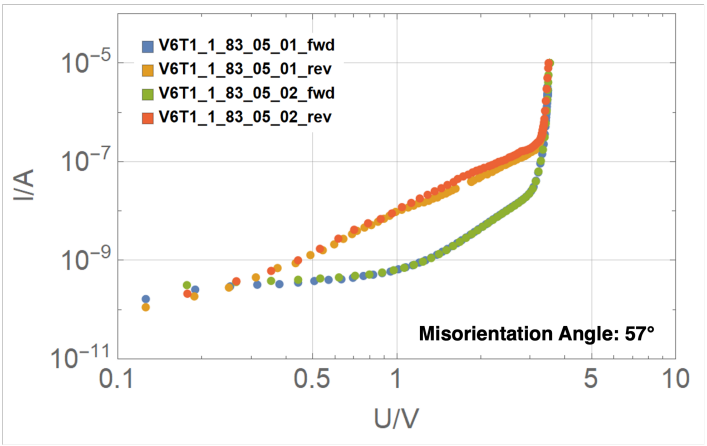

(c) Asymmetric I-V characteristic (V6T1#83 GB5).

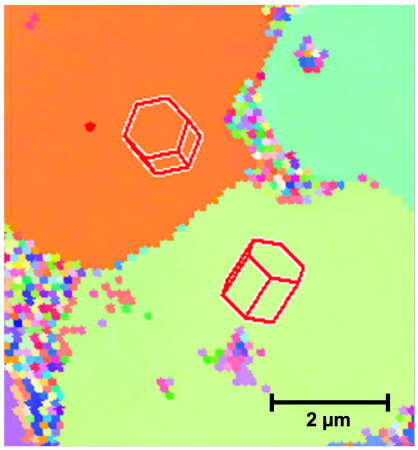

(d) EBSD scan of grain boundary 5.

Figure 4.4: Asymmetric I-V characteristics of grain boundaries with EBSD scans corresponding to archetype 1.

In Figure 4.5, different asymmetrical I-V characteristics and EBSD scans of grain boundaries corresponding to Archetype 2 are shown. The first grain boundary presented in this Figure, 4.5(a), does not align well with archetype 2 (see EBSD scan in Figure 4.5(b)), while the other two show a good fit. This is corroborated by corresponding EBSD scans, shown for the latter two grain boundaries in Figures 4.5(f) and 4.5(d). The grain boundary in Figure 4.5(b) exhibits less polar interfaces at the grain boundary, since the polar c-axes are tilted away from the grain boundary. Thus, a less asymmetrical I-V characteristic compared to the other two grain boundaries is expected and seen in the respective measurement in Figure 4.5(a).

In Figure 4.6(a), an asymmetrical I-V characteristic of a grain boundary with an EBSD scan corresponding to Archetype 3 is shown. As in this archetype, the polar c-axes facing the interface are both oxygen-terminated (tail-to-tail alignment), the I-V characteristic is

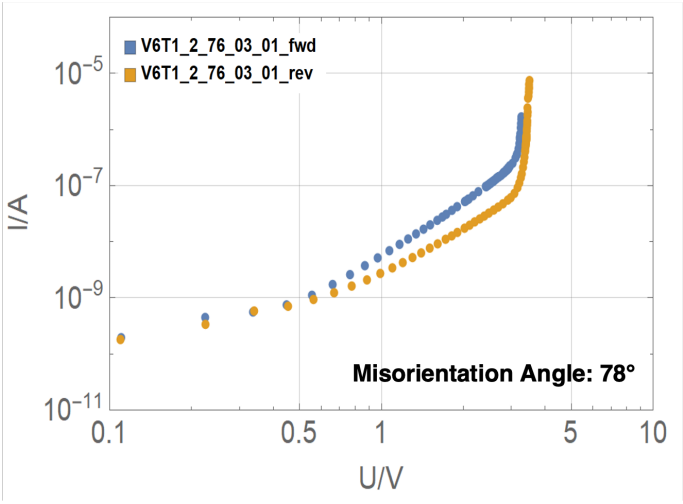

(a) Asymmetric I-V characteristic (V6T1#76 GB3)

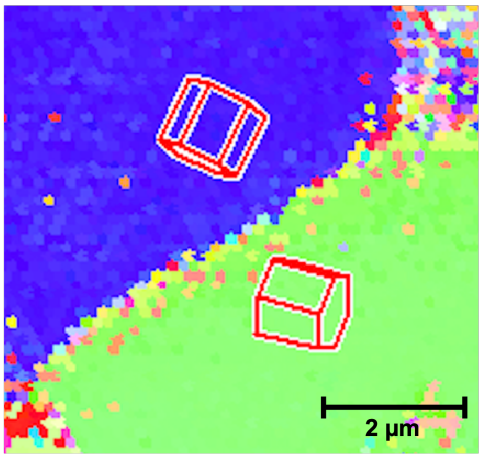

(b) EBSD scan of grain boundary 3.

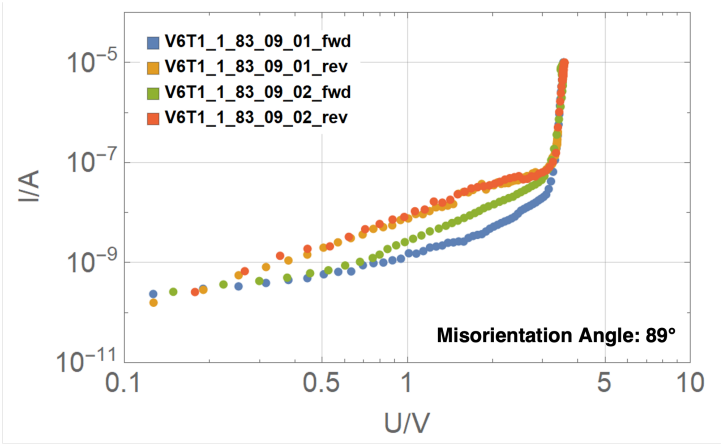

(c) Asymmetric I-V characteristic (V6T1#83 GB9).

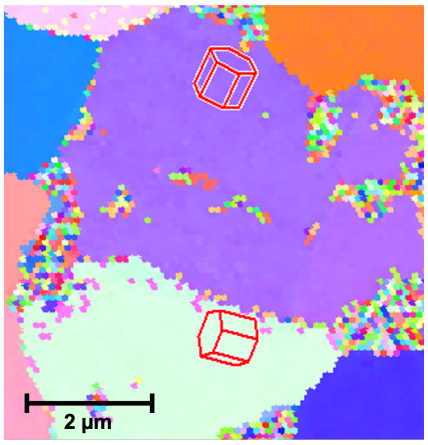

(d) EBSD scan of grain boundary 9.

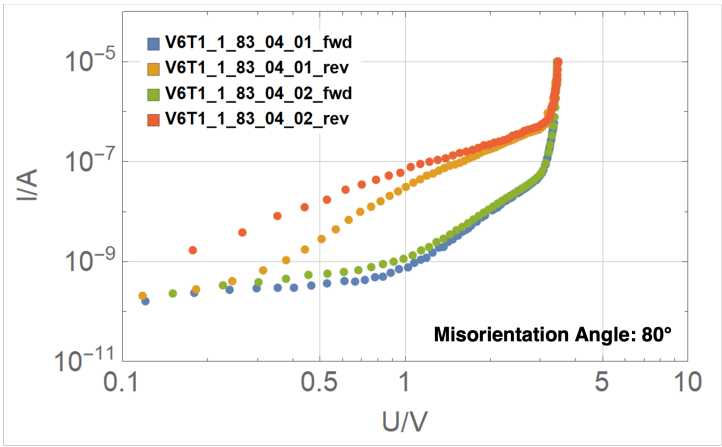

(e) Asymmetric I-V characteristic (V6T1#83 GB4).

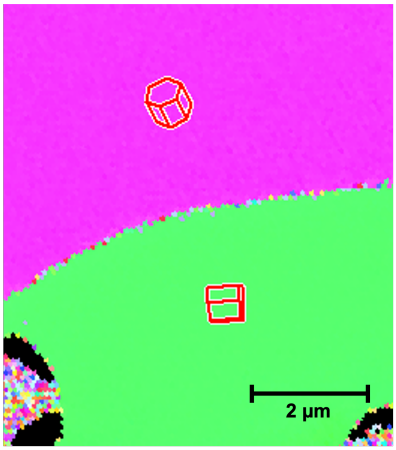

(f) EBSD scan of grain boundary 4.

Figure 4.5: Asymmetric I-V characteristics of grain boundaries with EBSD scans corresponding to Archetype 2.

expected to be symmetrical, as described in [28]. However, Figure 4.6(a) shows highly asymmetrical behaviour, the grains are also tilted with respect to the grain boundary (Figure 4.6(b)). This behaviour was also observed in tilted archetype 3 grains in [4].

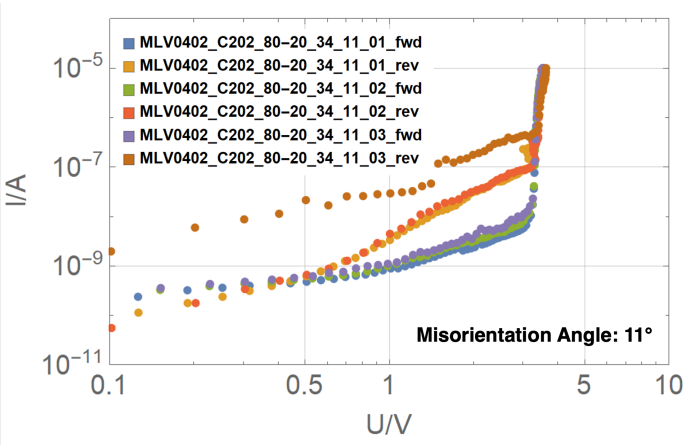

(a) Asymmetric I-V characteristic (MLV#34 GB11).

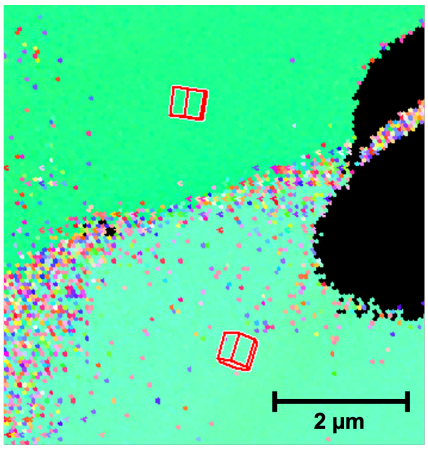

(b) EBSD scan of grain boundary 11.

Figure 4.6: Asymmetrical I-V characteristic of grain boundary with EBSD scan corresponding to archetype 3.

On one hand, the results in the preceding section, summarized in Table 4.2, also align well with data measured and analysed in [4]. On the other hand, the results in this section also highlight the need for additional specimen preparation and characterization detailed in section 4.1.1 for definitive conclusions on the grain orientation. The issue of not knowing the grain boundary orientation below the surface can also be addressed by using bicrystal grain boundaries with well-defined orientations corresponding perfectly to the proposed archetypes, as was done for example by Cheng in [3].

Table 4.2: Summary of grain boundaries with asymmetrical I-V characteristics. The sample and grain boundary (GB) number, proposed archetype and misorientation are given. Additionally, an assessment of alignment with the proposed archetype (either good or bad) is given.

Sample No.	GB No.	Proposed Archetype	Misorientation Angle	Aligment with Archetype
V6T1#83	11	mantle-to-mantle	46°	good
V6T1#83	5	mantle-to-mantle	57°	good
V6T1#76	3	mantle-to-tail	78°	bad
V6T1#83	4	mantle-to-tail	80°	good
V6T1#83	9	mantle-to-tail	89°	good
MLV#34	11	tail-to-tail	11°	bad

4.2 APT Investigation of Bulk Material and Parameter Study

The measurements of the bulk material were obtained from MLV and EV samples. In total, six bulk measurements of MLV and EV samples were carried out, of which two yielded results. To improve the quality of the mass spectra, a parameter study was carried out.

The varied parameters are described as follows:

1. Temperature: 40, 50 or 60 K
2. Measurement Mode (Laser or Voltage):
    a) Voltage Mode:
        i. Pulse Frequency: 200 kHz
    b) Laser Mode:
        i. Laser Energy: 0.2, 0.4 or 0.6 nJ
        ii. Laser Frequency: 200 or 250 kHz

Voltage measurements were carried out at 60 K and 200 kHz, but all samples fractured at the beginning of the measurement and no results were obtained. Laser measurements were carried out at 200 and 250 kHz and different laser energies of 0.2, 0.4 and 0.6 nJ. Furthermore, the temperature was also studied from 40 to 60 K with a step-size of 10 K. The results of the laser measurements are presented in Table 4.3.

The best results were obtained in laser mode with a higher frequency and lower energy of 250 kHz and 0.2 nJ, respectively, resulting in three successful measurements. Alternatively, a lower frequency and higher energy of 200 kHz and 0.6 nJ can also be used, which resulted in one successful measurement. The sample temperature was varied from 40 - 60 K and does not affect the background of the measurement.

For the quantification of the chemical composition of the specimens peak deconvolution was carried out. This was previously done by Dawahre and Shen in [26] to separate overlapping peaks in the mass spectrum, improving the initial Zn:O ratio of 79:21 to 1:1.04. Thus, a separation of overlapping peaks allows obtaining an accurate chemical quantification. The peak deconvolution resulted in significantly high deviation to the initial powder composition. A very high background was observed in all APT measurements. In order to achieve lower background and to get a better fit to the initial powder composition, the best measurements after the parameter study were selected for further analysis.

A comparison of a non-deconvoluted and a deconvoluted measurement of the bulk material (sample V6T1#76) is shown in Table 4.4. The zinc-oxygen ratio decreases from 77:21 to

Table 4.3: Parameter study of conducted APT measurements in laser mode. Measurements 1, 2, 4 and 8 were successful and the results are discussed in this thesis.

Measurement No.	Temperature [K]	Frequency [kHz]	Energy [nJ]	Quality
1	60	200	0.6	successful (bulk)
2	40	250	0.2	successful (GB)
3	40	200	0.2	failed
4	50	250	0.2	successful (bulk)
5	50	250	0.6	failed
6	50	250	0.6	failed
7	50	250	0.4	failed
8	40	250	0.2	successful (GB)

37:63, while bismuth is only detected after deconvolution. Compared to the initial powder composition, both the original and the deconvoluted measurement show a discrepancy between the expected stochiometry and the obtained results. Thus, all measured element concentrations should be interpreted qualitatively. Dopants such as antimony, chromium and aluminum are not detected in either the original measurement or the deconvolution. The concentration of all other dopant elements such as cobalt, manganese, nickel and silicon decreases after deconvolution. All following Tables present only the deconvoluted measurements.

Table 4.4: Comparison of initial composition and results of an atom probe measurement of the bulk material, both without and with peak deconvolution, for measurement No. 1 (sample V6T1#76). The deviation in at.% in the Total sum is due to rounding errors.

Element	Initial [at.%]	V6T1#76 (No. 1), original [at.%]	V6T1#76 (No. 1), deconv. [at.%]
Zinc (Zn)	45.3934	77.55	36.672
Oxygen (O)	50.8226	21.42	63.123
Bismuth (Bi)	0.9565	-	0.009
Cobalt (Co)	0.4927	0.36	0.025
Manganese (Mn)	0.2348	0.10	0.082
Antimony (Sb)	0.9565	-	-
Chromium (Cr)	0.4636	-	-
Nickel (Ni)	0.4858	0.13	0.079
Silicon (Si)	0.1910	0.01	0.011
Aluminum (Al)	0.0029	-	-
Total	99.9998	99.57	99.976

In Table 4.5, the deconvoluted results of the atom probe measurements of the bulk material composition are presented and compared with the initial powder composition. All measurements are depicted in atomic percentage (at.%). The initial concentrations were calculated from Table 3.2 as follows: first, the oxygen percentage for each molecule is calculated. This is done by multiplying the cation percentage in Table 3.2 by the oxygen ratio of the respective molecule. For Bi_2O_3, the oxygen ratio would be 3/2 and the cation percentage 1.9452. The oxygen percentages of all molecules are added to obtain the total oxygen percentage (103.3472%). This is then added to the total cation percentage (100.0018%) to obtain the total percentage (203.3490%). For each element, the initial concentration in at% can now be calculated by dividing the cation percentage or, in the case of oxygen, the total oxygen percentage, by the total percentage.

Even though atom probe tomography allows for detection of atoms down to levels under 100 ppm [29], elements such as aluminum, antimony, which is added to reduce grain size and chromium, which increases nonlinear I-V behaviour [2], were not detected. Aluminum is added in very small quantities and therefore it is expected to not be detected in the deconvoluted measurement. Antimony is segregated in the spinel phase as $Zn_7Sb_2O_{12}$ [27, 30], therefore it is not expected to be detected in a measurement of the bulk material. Generally, a smaller percentage of dopant elements such as Co, Mn, Ni and Si is found deconvoluted measurements. This can be explained by their segregation to and around the Sb-spinel, as examined in [27]. Since antimony and silicon act as grain growth inhibitors, they form mostly spinel and and pyrochlore phases [1]. Bismuth is mainly found in intergranular phases at the grain boundaries, for example as $\beta - Bi_2O_3$ [27]. In the deconvoluted measurements, the concentration of the dopant elements is lower.

Table 4.5: Comparison of initial composition and results of atom probe measurements of the bulk material with peak deconvolution. The deviation in at.% in the Total sum is due to rounding errors.

Element	Initial [at.%]	V6T1#76 (No. 1), deconv. [at.%]	MLV#34 (No. 4), deconv. [at.%]
Zinc (Zn)	45.3934	36.672	35.096
Oxygen (O)	50.8226	63.123	62.423
Bismuth (Bi)	0.9565	0.009	0.018
Cobalt (Co)	0.4927	0.025	0.025
Manganese (Mn)	0.2348	0.082	0.065
Antimony (Sb)	0.9565	-	-
Chromium (Cr)	0.4636	-	-
Nickel (Ni)	0.4858	0.079	0.083
Silicon (Si)	0.1910	0.011	0.002
Aluminum (Al)	0.0029	-	-
Total	99.9998	99.976	97.712

4.3 Characterization of Grain Boundaries

In order to characterize grain boundaries, an I-V measurement is carried out. To determine the grain boundary orientations, an EBSD scan was done. Following this, the grain boundary is lifted out using FIB and characterized with TKD, as described in section 3.2. Using this method, two grain boundaries were analysed with APT and are discussed in the following section. The bulk composition of both these measurements is shown in Table 4.6. The results of the APT experiments are discussed in the next section, followed by a comparison of both grain boundary concentration profiles.

Generally, after the peak deconvolution, all dopant elements show a reduction in concentration, this effect was also present in the analysis of the bulk material (see Table 4.5). The grain boundary composition analysis shows a higher concentration of bismuth compared to the bulk material. Previous studies showed a segregation of bismuth to the grain boundaries [31], thus a rise in concentration at the grain boundary is expected. All other elements have comparable concentrations in both the bulk and the grain boundary analysis.

Table 4.6: Comparison of initial composition and results of atom probe measurements of grain boundaries with peak deconvolution. The deviation in at.% in the Total sum is due to rounding errors and the omission of certain elements.

Element	Initial [at.%]	V6T1#83 (No. 8), deconv. [at.%]	MLV#34 (No. 2), deconv. [at.%]
Zinc (Zn)	45.3934	37.760	40.621
Oxygen (O)	50.8226	62.052	59.226
Bismuth (Bi)	0.9565	0.037	0.005
Cobalt (Co)	0.4927	0.015	0.022
Manganese (Mn)	0.2348	0.064	0.061
Antimony (Sb)	0.9565	-	-
Chromium (Cr)	0.4636	-	-
Nickel (Ni)	0.4858	0.055	0.060
Silicon (Si)	0.1910	0.017	0.006
Aluminum (Al)	0.0029	-	-
Total	99.9998	99.976	97.712

4.3.1 Grain Boundary with asymmetrical I-V Characteristic

To start the characterization process of this grain boundary taken from an energy varistor (sample V6T1#83), a I-V measurement was carried out of the grain boundary to be lifted-out, see Figure 4.7(a). Using the FIB, an SEM picture (Figure 4.7(b)) and an EBSD scan (Figure 4.7(c)) were taken. The archetype was confirmed to be archetype 2. The twin boundaries in the REM picture indicate a mantle-to-tail orientation between the two grains, as the polar axis in this material is always orientated towards the twin boundary [18]. The EBSD scan was used to measure the misorientation angle, which was 80° for this grain boundary. This indicates a high conformity to the archetype. As such, an asymmetrical I-V characteristic is expected and confirmed through the 4-pole measurement.

This characterization was followed up with the lift-out and tip preparation detailed in section 3.3.2. The TKD scan confirmed the grain boundary in the tip as well as the misorientation angle of 80° and is shown in Figure 4.8.

The mass spectrum for the APT measurement of this sample is depicted in Figure 4.9. A reconstruction with all identified atoms is shown in Figure 4.10(a). Two concentration profiles were investigated orthogonal through the grain boundary (Positions 1 and 2). These positions are marked with an X in Figure 4.10(b). All concentration profiles were taken from the left to the right side of the sample. It is important to note that all concentration profiles were generated from the original, e.g. uncorrected data without peak deconvolution and therefore, they can only be analysed qualitatively. Bismuth is one of the dopant elements that segregate to the grain boundary [11], and an individual reconstruction including only Bi atoms can be seen in Figure 4.10(c). The grain boundary, with a higher concentration of Bi atoms, can be discerned clearly in darker red. The bismuth peak in the concentration profile (7 nm, see Figure 4.13) was used as a reference for the width of the grain boundary.

Figure 4.11 depicts concentration profiles of oxygen and zinc through the grain boundary, namely positions 1 and 2 in Figure 4.10(b). A trend of inverse concentrations in the range of 2 at% for zinc and oxygen is seen in every concentration profile, with oxygen atoms segregating to the right side, while zinc atoms segregate to the left side. In the literature, only zinc depletion in the grain boundary was reported [3], however, this was only done on bicrystals with a barrier width of 25 μm. In the case of this grain boundary, the grain boundary misorientation and archetype (mantle-to-tail) leading to an asymmetrical I-V characteristic indicate that one side of the interface is zinc-terminated. The inverse zinc and oxygen concentrations on both sides of the grain boundary might point to this being the case, nevertheless, the same findings are reported in section 4.3.2 for a grain boundary with a symmetrical I-V characteristic.

Following, concentration profiles for every detected dopant element were generated. Man-

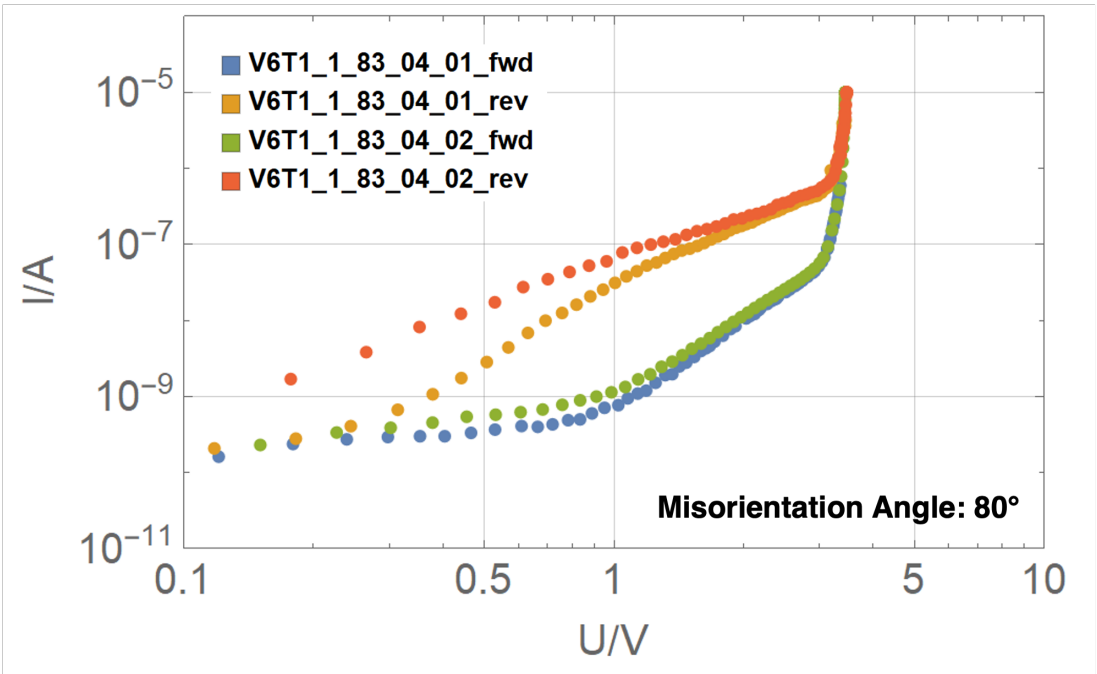

(a) Asymmetric I-V characteristic of grain boundary, clearly confirmed by both measurements.

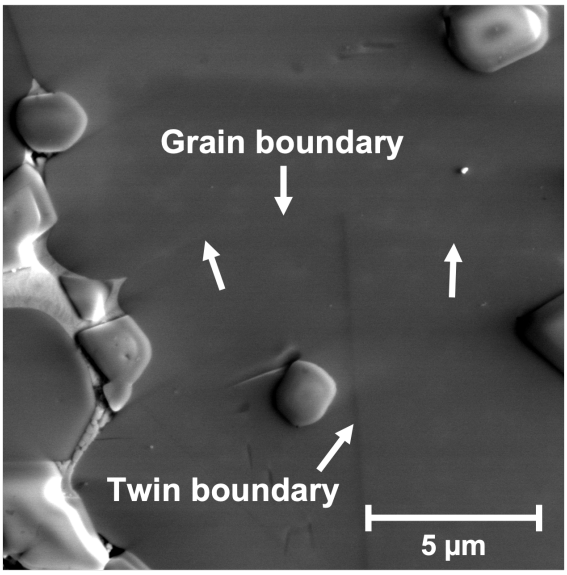

(b) SEM picture of grain boundary, marked with three white arrows. A twin boundary is also marked in the picture, notably absent from the EBSD scan.

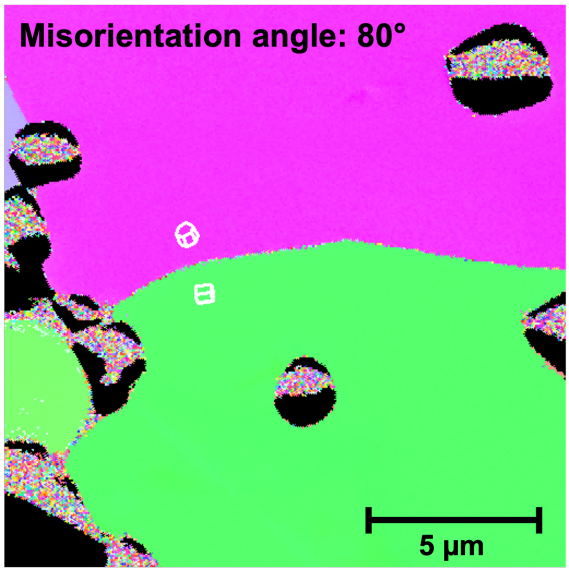

(c) EBSD Scan of grain boundary. The white hexagons illustrate the mantle-to-tail orientation of the grain boundary.

Figure 4.7: I-V Characteristics, SEM and EBSD pictures of an asymmetrical grain boundary, which was later lifted out and analysed using APT.

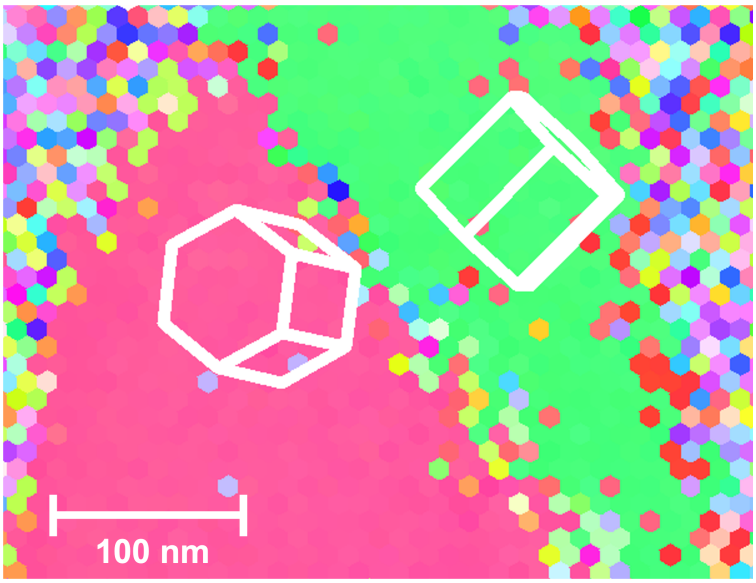

Figure 4.8: EBSD scan of the tip, annular milled using the ion source of the FIB. White hexagons illustrate the orientation relationship between the two grains. The misorientation angle was confirmed to be 80°, as in 4.7(c).

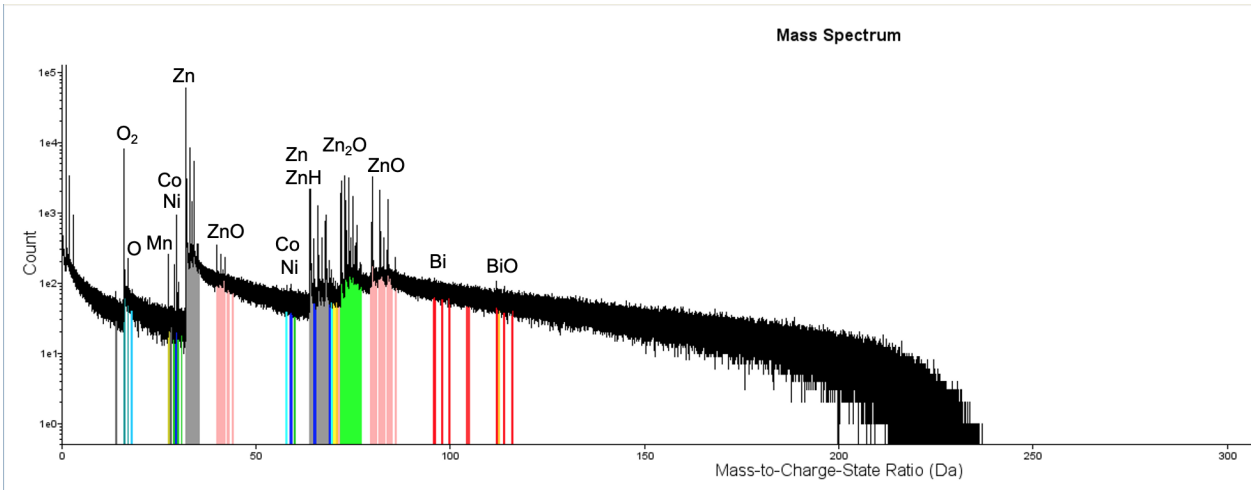

Figure 4.9: Mass spectrum of APT measurement No. 8, sample V6T1#83.

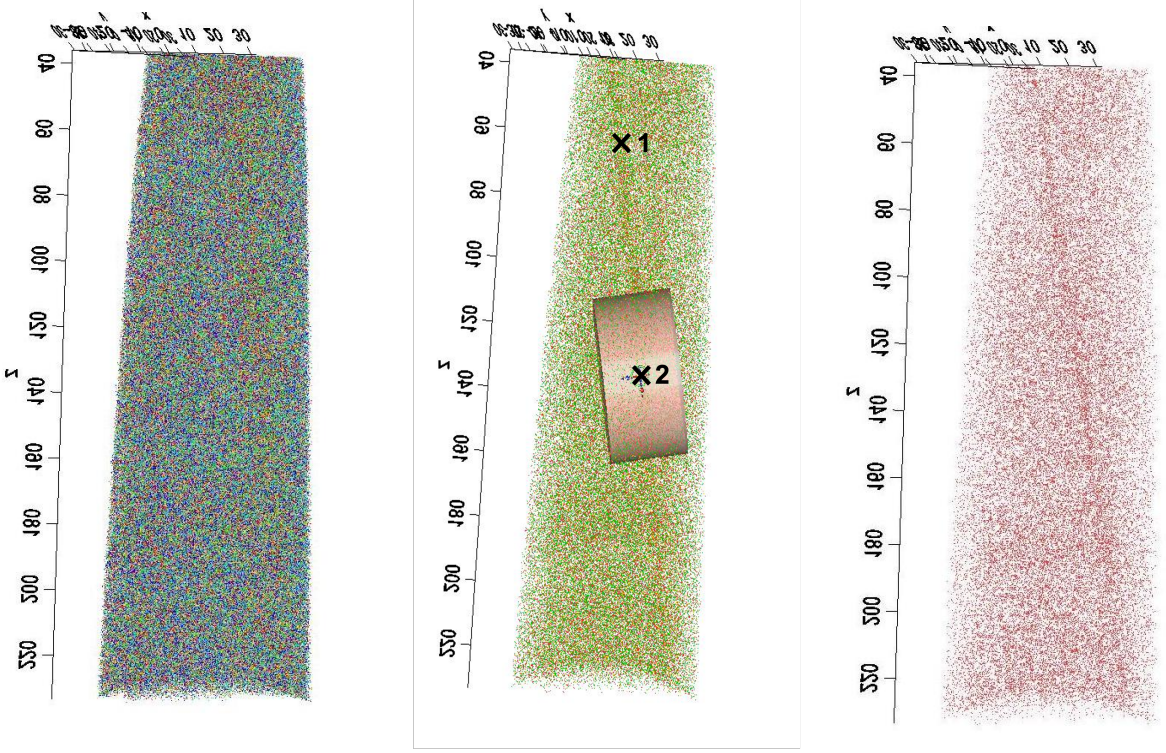

(a) APT reconstruction of grain boundary with an asymmetrical I-V characteristic, all atoms shown. The grain boundary is not immediately visible.

(b) APT reconstruction of grain boundary with an asymmetrical I-V characteristic. Positions where the concentration profile was analysed are marked with a black X and their number, a sample concentration profile cylinder is included. Only atoms with a higher concentration in the grain boundary (Bi, Ni, Si) are shown.

(c) APT reconstruction of grain boundary with an asymmetrical I-V characteristic, only Bismuth atoms shown. The grain boundary can be seen clearly in a darker red, where the Bismuth concentration is higher.

Figure 4.10: APT reconstructions of grain boundary with an asymmetrical I-V characteristic. The scale of all axis labels is given in nm. The concentration profiles in (b) were taken from left to right.

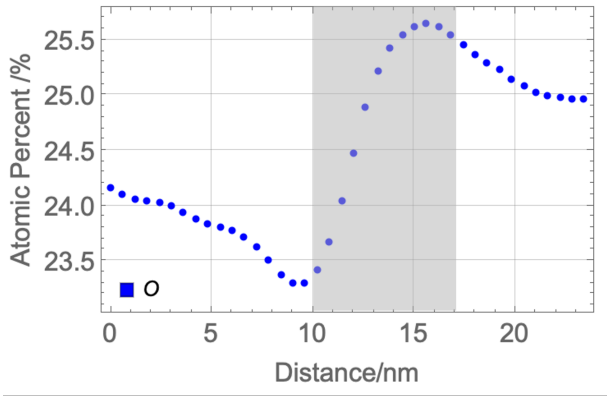

(a) Concentration profile of oxygen for position 1 (top).

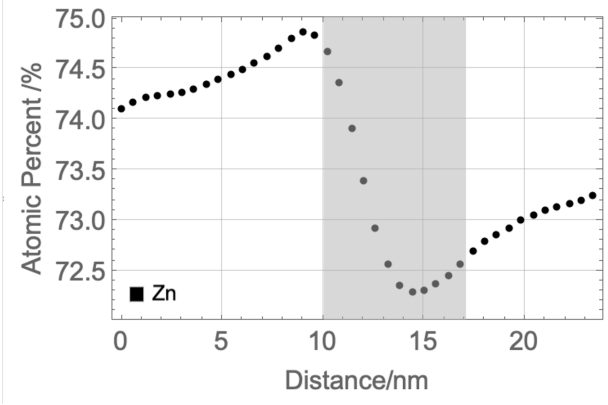

(b) Concentration profile of zinc for position 1 (top).

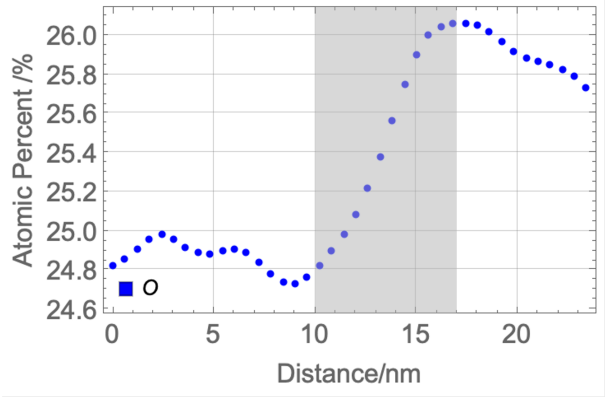

(c) Concentration profile of oxygen for position 2 (middle).

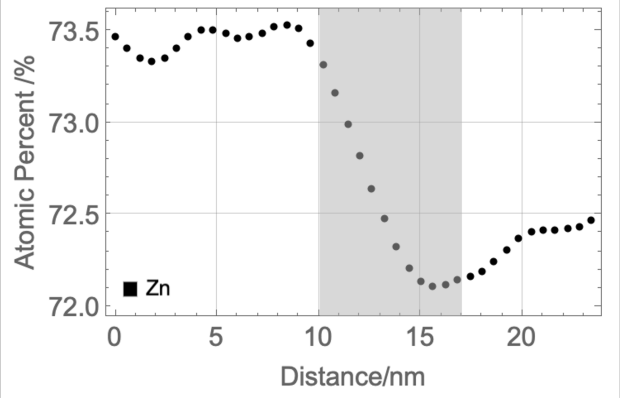

(d) Concentration profile of zinc for position 2 (middle).

Figure 4.11: Concentration profiles of oxygen and zinc through the grain boundary, positions 1 and 2 (top and middle). The grain boundary is indicated in grey.

ganese (Mn) and nickel (Ni) were excluded from the analysis, as their concentration profiles proved to be inconclusive, e.g. no meaningful peaks could be discerned. In the case of manganese, this is backed up by evidence that manganese does not segregate at the grain boundaries and thus would have a uniform concentration profile [31]. Figure 4.12 shows concentration profiles for silicone (Si) and cobalt (Co) for positions 1 and 2 (top and middle) through the grain boundary. Wu *et al* showed that silicone was present in both grain boundary and the grain itself, either substituting Zn in ZnO or segregating as SiO_2 glass phase or spinel phase at the grain boundary [32]. Cobalt has been found to dissolve fully in the ZnO phase [33], replacing Zn in the lattice. However, both elements segregate at the grain boundary, with a doubled concentration in the grey region marking the grain boundary.

The concentration profile of Bismuth (Bi) is depicted in Figure 4.13. A clear peak in the grain boundary region can be discerned, with nearly double the concentration of bismuth inside the grey region. The highest bismuth concentration can be found within an area of

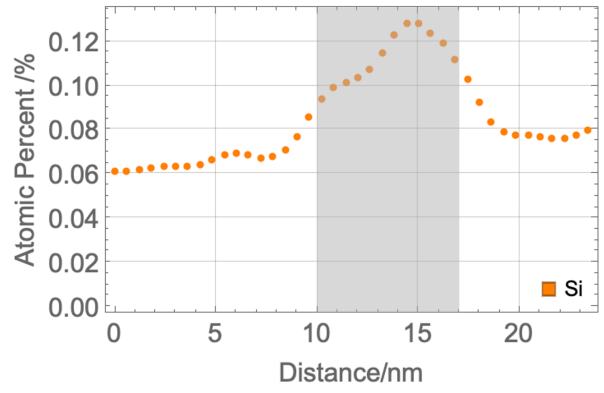

(a) Concentration profile of silicon for position 1 (top).

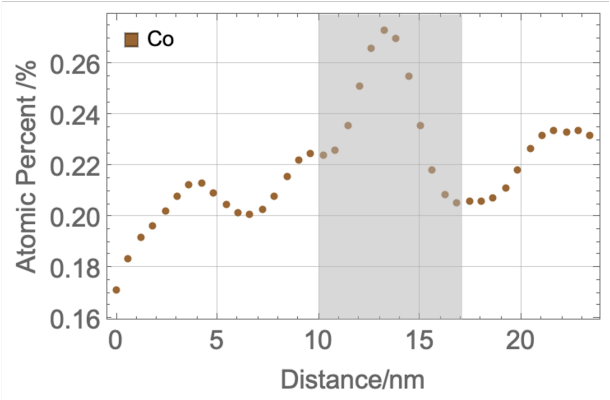

(b) Concentration profile of cobalt for position 1 (top).

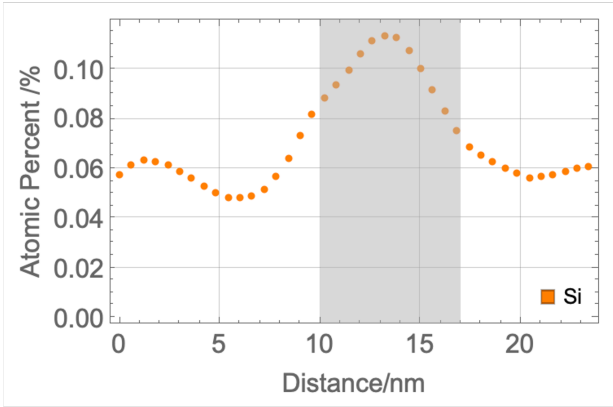

(c) Concentration profile of silicon for position 2 (middle).

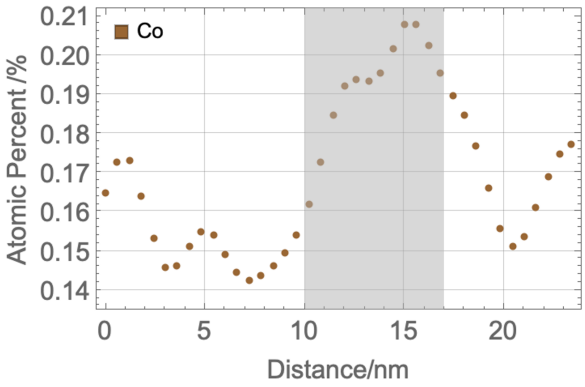

(d) Concentration profile of cobalt for position 2 (middle).

Figure 4.12: Concentration profiles of silicon and cobalt through the grain boundary, positions 1 and 2 (top and middle). The grain boundary is indicated in grey.

1-2 nm, aligning well with literature findings of a 1-2 nm wide bismuth segregation region at the grain boundary [1]. Owing to its larger atomic radius, bismuth is virtually insoluble in ZnO grains and segregates to the grain boundaries, where the larger atoms substitute Zn in spaces that present longer Zn-O bond lengths [5]. Interestingly, in our analysis, bismuth does not segregate fully to the grain boundaries and is still present in the bulk material (see Figure 4.5), albeit in a lesser concentration.

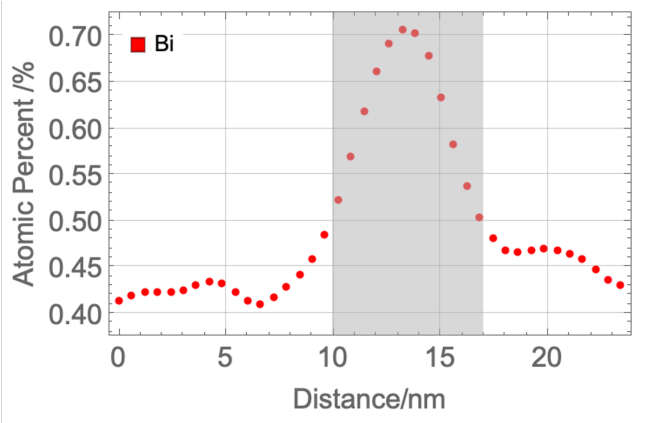

(a) Concentration profile of bismuth for position 1 (top).

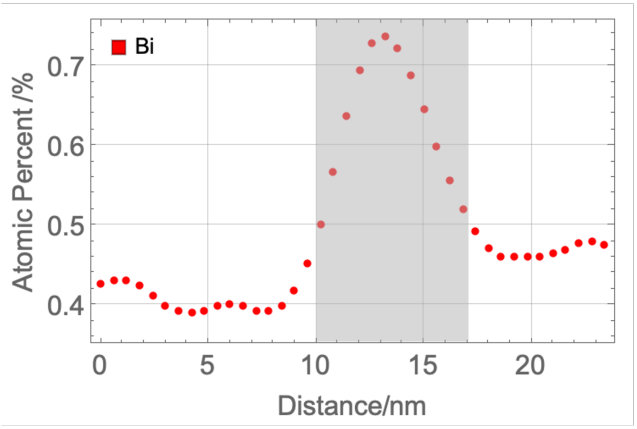

(b) Concentration profile of bismuth for position 2 (middle).

Figure 4.13: Concentration profiles of bismuth through the grain boundary, positions 1 and 2 (top and middle). The grain boundary is indicated in grey.

4.3.2 Grain Boundary with symmetrical I-V Characteristic

This grain boundary was taken from a MLV (sample MLV#34). Firstly, a I-V measurement was carried out of the grain boundary to be lifted-out, see Figure 4.7(a). Using the FIB, an SEM picture (Figure 4.7(b)) and an EBSD scan (Figure 4.7(c)) were taken. The high contamination rate of EBSD scan can be attributed to scratches on the sample surface and the low emission current of the microscope at the time of the analysis. The archetype was confirmed to be archetype 3. The SEM picture also shows twinning in both grains, which allows for identification of a tail-to-tail orientation between the two grains, as in [18]. The EBSD scan was used to measure the misorientation angle, which was 32° for this grain boundary. The EBSD scan indicates a high conformity to the archetype. As such, an symmetrical I-V characteristic is expected and confirmed through the 4-pole measurement.

The characterization was followed up with a lift-out and tip preparation detailed in section 3.3.2. The TKD scan confirmed the grain boundary in the tip as well as the misorientation angle of 32° and is shown in Figure 4.15.

The mass spectrum for the APT measurement is depicted in Figure 4.16. A reconstruction with all identified atoms is shown in Figure 4.17(a). This was followed up with a concentration profile through the grain boundary (Figure 4.17(b)), from the right to the left side of the sample. As the grain boundary was located quite close to the edge of the sample, no further concentration profiles were taken. It is important to note that with this sample, the concentration profile was also generated from the original, e.g. uncorrected, data without peak decomposition. Therefore it can also only be analysed qualitatively. An individual reconstruction including only Bi atoms can be seen in Figure 4.17(c). The grain boundary, with a higher concentration of Bi atoms, can be discerned faintly in richer petrol. For the width of the grain boundary, the peak of the Bismuth concentration profile (7 nm, see Figure 4.18(e)) was used as a reference, to ensure comparability with the previous grain boundary.

Subsequently, concentration profiles for oxygen, zinc and every detected dopant element were generated. Manganese (Mn) and nickel (Ni) were again excluded from the analysis, as their concentration profiles also proved to be not of relevance for the same reasons given in the previous subsection.

Figures 4.18(a) and 4.18(b) depict concentration profiles of oxygen and zinc, respectively, through the grain boundary, for position 1 in Figure 4.17(b). The trend of inverse concentrations in the range of 2 at% for zinc and oxygen is repeated in this grain boundary, with oxygen atoms segregating to the left side, while zinc atoms segregate to the right side. According to the archetype (3, tail-to-tail, see Figure 4.14(c)) and the I-V measurement (symmetric, see Figure 4.14(a)), this grain boundary should lack polarity, however, the difference in zinc and oxygen concentrations on both sides of the interface are in the same range as with the previ-

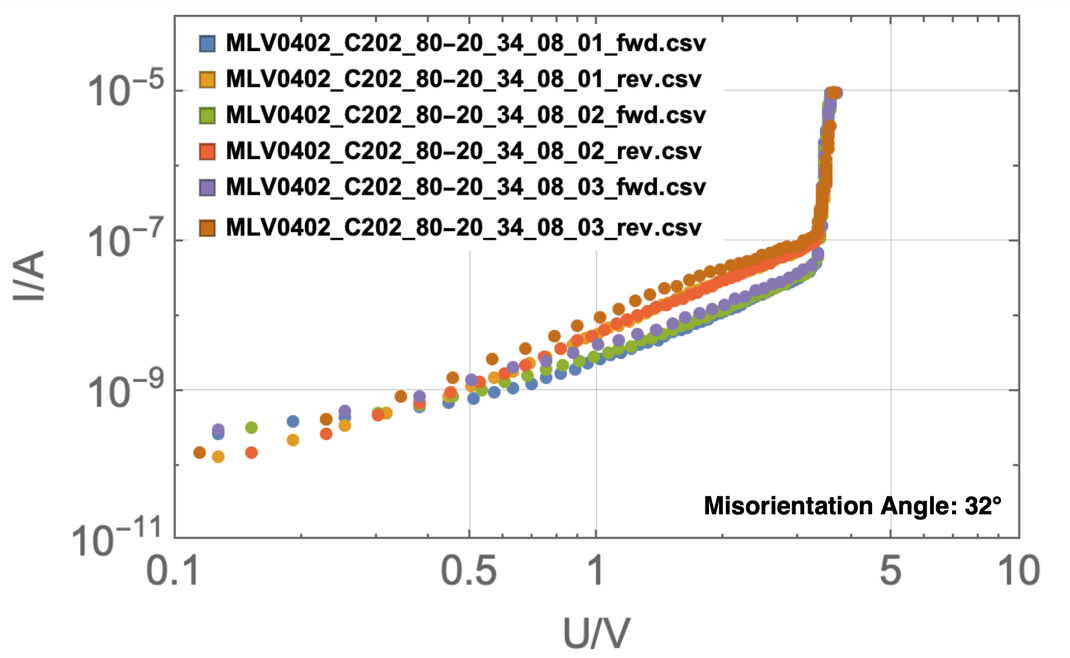

(a) Symmetric I-V characteristic of grain boundary, clearly confirmed through three measurements.

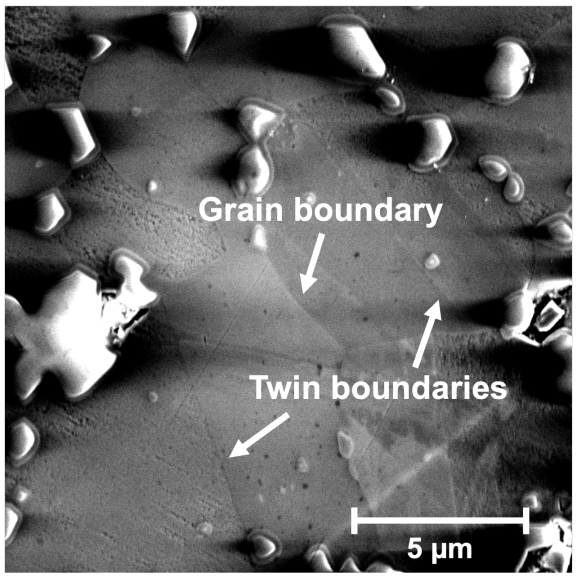

(b) SEM picture of grain boundary, marked with three white arrows. Scratches arising from the polishing process that later also occur in the EBSD scan can be seen as grey lines next to the grain boundary.

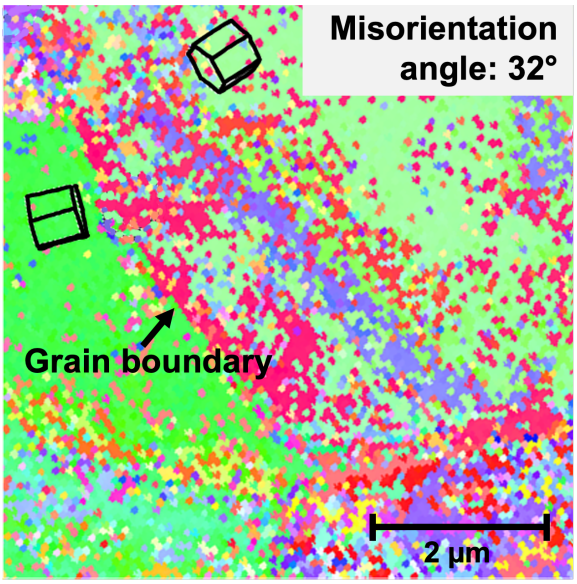

(c) EBSD Scan of grain boundary. The black hexagons illustrate the tail-to-tail orientation of the grain boundary. The red and purple areas are scratches that occured during the preparation process and are rated as contamination.

Figure 4.14: I-V Characteristics, SEM and EBSD pictures of a symmetrical grain boundary, which was later lifted out and analysed using APT.

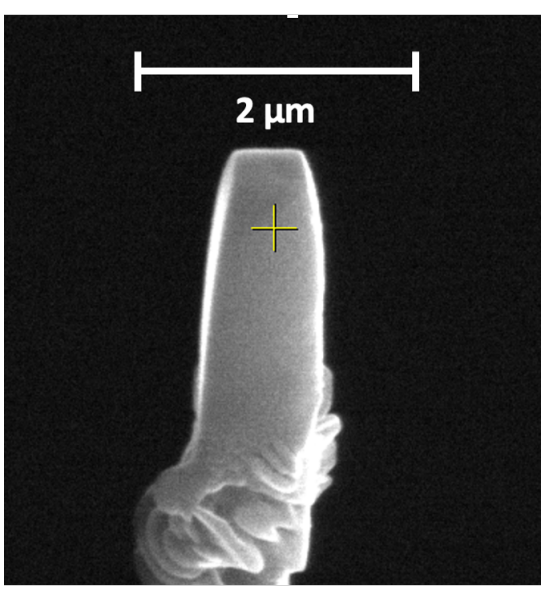

(a) Picture of the glued-on tip taken in the SEM before annular milling.

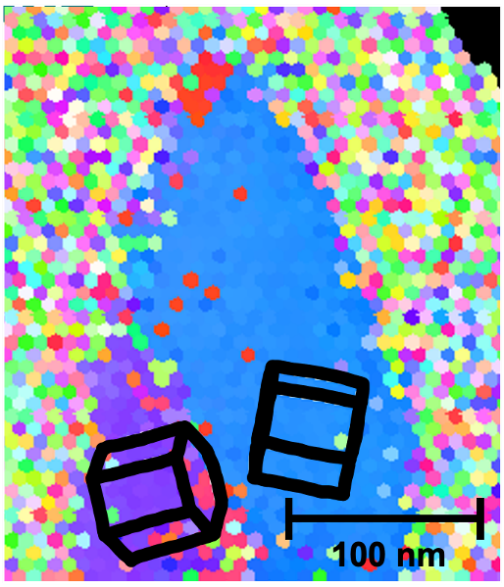

(b) EBSD Scan of grain boundary. The black hexagons illustrate the tail-to-tail orientation of the grain boundary. The red and purple areas are scratches that occured during the preparation process and are rated as contamination.

Figure 4.15: SEM picture (a)) and EBSD scan (b)) of the tip.

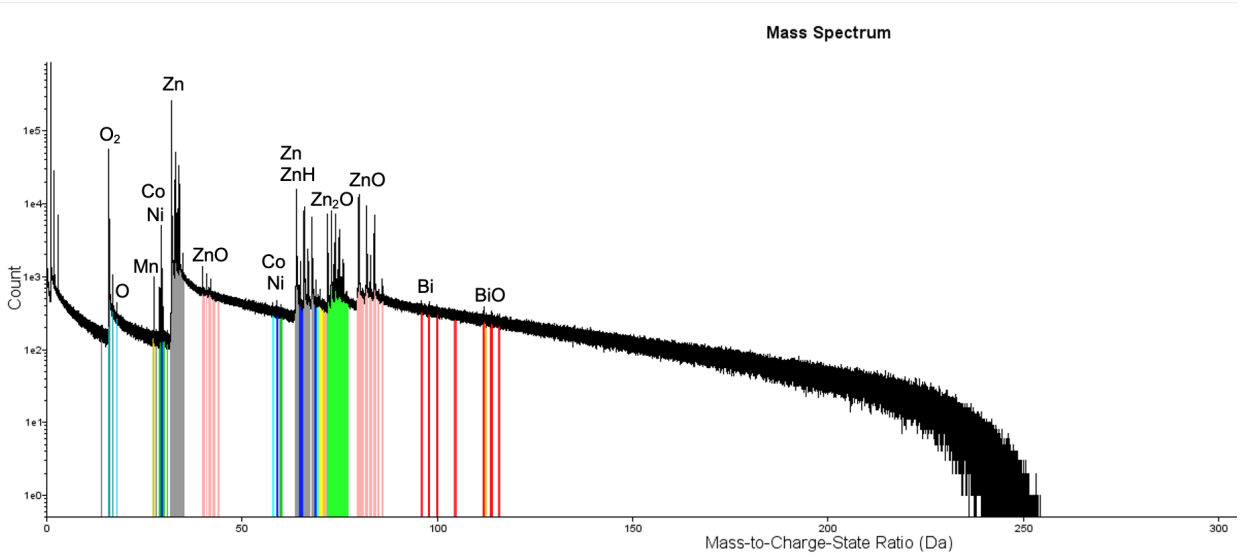

Figure 4.16: Mass spectrum of APT measurement No. 2, sample MLV#34.

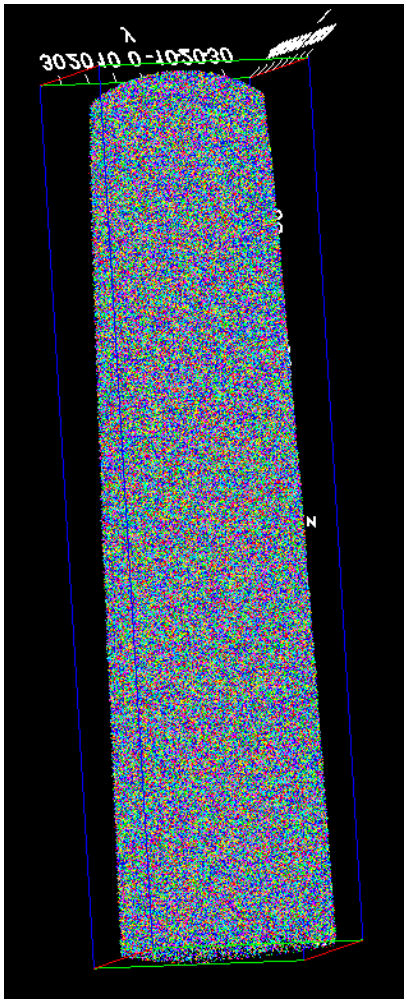

(a) APT reconstruction of grain boundary with symmetrical I-V characteristic, all atoms shown. The grain boundary is not immediately visible.

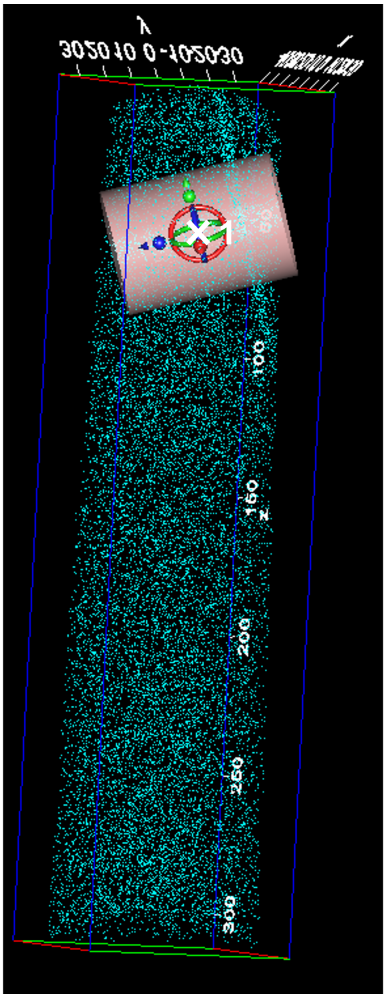

(b) APT reconstruction of grain boundary with a symmetrical I-V characteristic. The position where the concentration profile was analysed is marked with a white X1, a sample concentration profile cylinder is included. Only BiO molecules are shown for higher visibility.

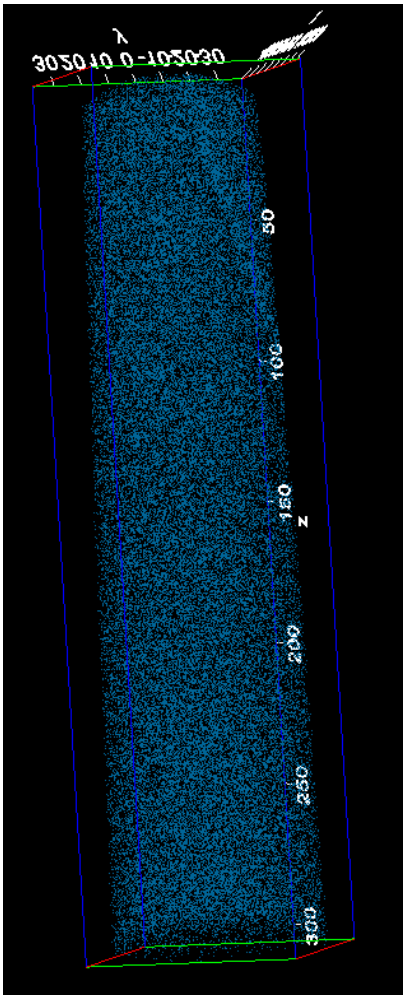

(c) APT reconstruction of grain boundary with a symmetrical I-V characteristic, only Bismuth atoms shown. The grain boundary is visible in the upper right corner, in a richer petrol colour.

Figure 4.17: APT reconstructions of grain boundary with a symmetrical I-V characteristic. The scale of all axis labels is given in nm. The concentration profile in (b) was taken from right to left.

ous grain boundary. This suggests that an inverse oxygen-zinc concentration on the left and right side of the boundary is an inherent characteristic of grain boundaries in this material after an I-V measurement, irrespective of grain boundary orientation and archetype.

Figures 4.18(c), 4.18(d) and 4.18(e) show concentration profiles for silicone (Si), cobalt (Co) and bismuth (Bi) through the grain boundary. Silicone, as with the previous grain boundary, also segregates at the grain boundary, with a doubled concentration in the grey region marking the grain boundary. Cobalt shows no peak in the concentration profile in the grain boundary region, which is expected according to [33]. The bismuth peak in Figure 4.18(e) is of the same height and width as with the previous grain boundary, with a doubling of the concentration in the interface compared to the bulk material outside of the grain boundary.

The only difference in chemical composition between the grain boundary with an asymmetrical I-V characteristic and the grain boundary with a symmetrical I-V characteristic is the variation in cobalt content: The former shows a peak in cobalt content (Figure 4.12(b)), while the latter does not. The cobalt peak is, however, not as pronounced as the silicone (Figure 4.12(c)) or bismuth peaks (Figure 4.13(b)), for example. Generally, the missing cobalt peak in Figure 4.18(d) is not conclusive, since there is a high fluctuation in this particular concentration profile.

A more notable difference are the distinct grain orientations and thus archetypes of the two grain boundaries. The first grain boundary is of archetype 2 (mantle-to-tail), indicating polar charges at the interface, leading to an asymmetrical I-V characteristic. Contrarily, the second grain boundary can be classified as archetype 3 (tail-to-tail), with no distinct polarity present, leading to a symmetrical I-V characteristic.

The (a)symmetry of I-V characteristics thus most likely does not arise from the chemical composition at the grain boundary, but from the orientation relationship of the two adjacent grains, as demonstrated in section 4.1.

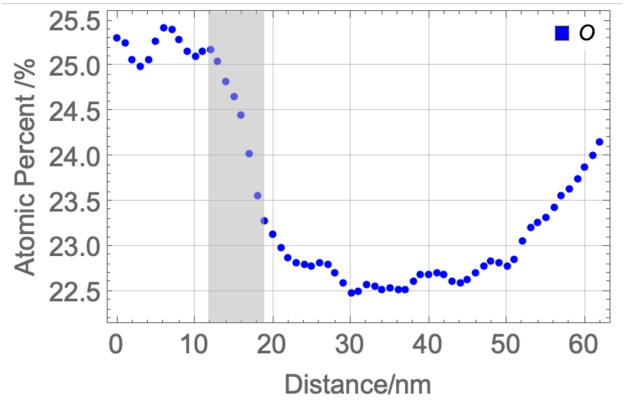

(a) Concentration profile of oxygen through the grain boundary.

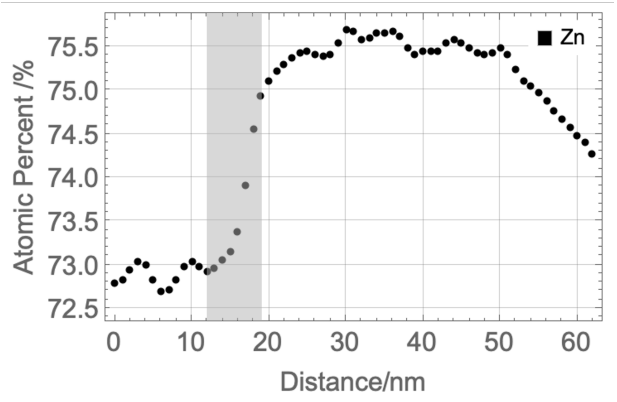

(b) Concentration profile of zinc through the grain boundary.

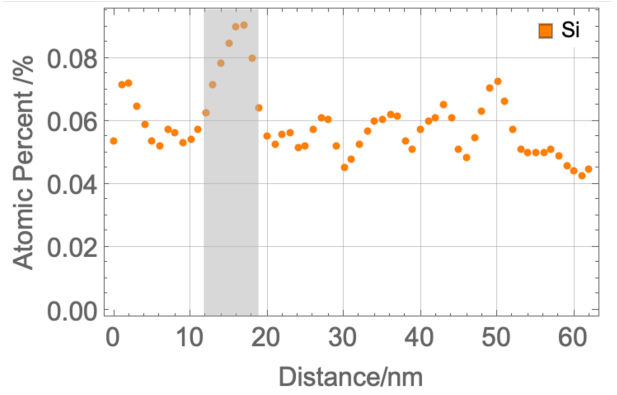

(c) Concentration profile of silicon through the grain boundary.

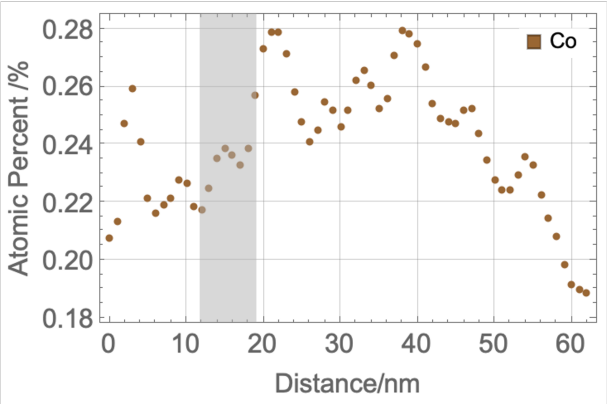

(d) Concentration profile of cobalt through the grain boundary.

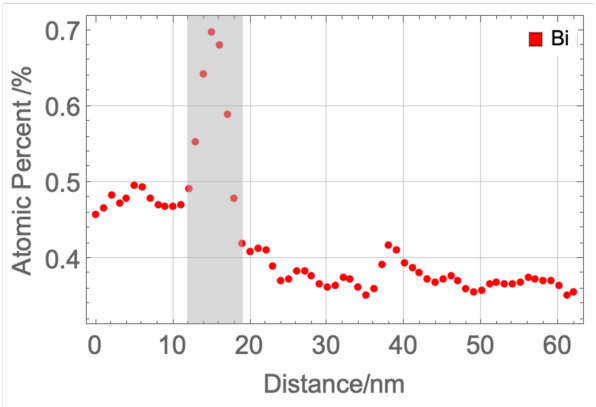

(e) Concentration profile of bismuth through the grain boundary.

Figure 4.18: Concentration profiles of oxygen, zinc, silicon, cobalt and bismuth through grain boundary with symmetrical I-V characteristic. The grain boundary is indicated in grey.

Chapter 5

Conclusion

In this work, varistor grain boundaries were characterized through their I-V characteristics and classified into three archetypes using EBSD scans. Asymmetrical and symmetrical I-V characteristics were recorded, dependant on the polarity of the grain boundary interface. Following, APT tips were prepared, with which bulk and grain boundary measurements were undertaken. The composition of various element concentrations in the grain boundaries and of the bulk material was documented and compared with existing literature.

A novel approach to the characterization of ZnO multilayer varistors and the associated methodology was developed, formulated and documented. For the first time, I-V measured varistor grain boundaries and associated concentration profiles were documented using atom probe tomography, showing clear asymmetrical segregation of certain elements in the grain boundary.

The following conclusions can be drawn:

- *Electrical Characterisation of Grain Boundaries:* It was demonstrated that grain boundaries show either predominantly symmetrical (non-polar or symmetrical polar interface orientation) or predominantly asymmetrical (polar interface orientation or polar-non-polar interface orientation) I-V characteristics depending on the grain boundary misorientation in the EBSD scan. A clear correlation between the (a)symmetry of the I-V characteristic and the grain boundary misorientation can be only ascertained through further sample preparation and characterization described in section 4.1.1.

- *Methodology and Preparation Process:* Special care should be taken during the annular milling of the tip, where the grain boundary can be easily destroyed with voltages or milling durations that are too high. Additionally, Si microarrays are not recommended as scaffolding for the ZnO material tip, as they break very easily in the APT microscope.

Instead, the lifted-out sample should be glued onto pre-electropolished tips cut from molybdenum or steel.

- *Composition of Bulk Material:* Using APT, the chemical composition was analysed and compared to the initial powder composition. The results show that bismuth not only segregates in the grain boundaries but also in the bulk material in trace amounts after peak deconvolution. It should be mentioned that the used atom probe was not able to reproduce the expected stochiometry, especially the cation-anion ratio.
- *Composition of Grain Boundaries:* Both analysed grain boundaries show the same chemical composition and distribution of atoms in the grain boundary, with the exception of a higher concentration of cobalt in the grain boundary with the asymmetrical I-V characteristic. Zinc and oxygen each respectively show a higher concentration on one side of the grain boundary and a depletion on the other side.

The I-V characteristics and chemical composition of varistor grain boundaries continue to offer novel opportunities for characterization and microstructural design. Further work is needed to ascertain and extend the results of this thesis. This can be done for example by an I-V characterization of bicrystal structures or a confirmation of the cobalt concentration in grain boundaries using APT. Additionally, the inverse concentrations of oxygen and zinc on both sides of the grain boundary should be further investigated. In this context, it is recommended to extend the present study of APT parameters to reduce the high measurement background to ensure higher reliability of the experimental data. These issues may be addressed in a future publication.

Bibliography

[1] D. R. Clarke, Journal of the American Ceramic Society **82**, 485 (1999).

[2] H. Jinliang, *Metal Oxide Varistors: From Microstructure to Macro-Characteristics* (2019).

[3] C. Cheng, J. He, and J. Hu, Applied Physics Letters **101** (2012).

[4] N. Raidl, *Einfluss des Gefüges auf die elektrischen Eigenschaften von Varistoren*, Ph.D. thesis, Montanuniversität Leoben, Institute of Structural and Functional Ceramics (2017).

[5] M. Trapp, P. Keil, T. Frömling, J. Rödel, and H. . Kleebe, Journal of the American Ceramic Society **103**, 2817 (2020).

[6] S. Desgreniers, Physical Review B - Condensed Matter and Materials Physics **58**, 14102 (1998).

[7] H. Veseem M, Umar A, Metal Oxide Nanostructures and Their Applications , 1 (2010).

[8] C. Wöll, Progress in Surface Science **82**, 55 (2007).

[9] S. Zhang, S.-H. Wei, and A. Zunger, Physical Review B - Condensed Matter and Materials Physics **63** (2001).

[10] wikipedia, "Ceramic capacitor production route," (2020).

[11] K. Eda, IEEE Electrical Insulation Magazine **5**, 28 (1989).

[12] Y. Sato, J. Buban, T. Mizoguchi, N. Shibata, M. Yodogawa, T. Yamamoto, and Y. Ikuhara, Physical Review Letters **97** (2006).

[13] M. Alim, S. Li, F. Liu, and P. Cheng, Physica Status Solidi (A) Applications and Materials Science **203**, 410 (2006).

[14] G. Pike, S. Kurtz, P. Gourley, H. Philipp, and L. Levinson, Journal of Applied Physics **57**, 5512 (1985).

[15] J. X. Zhang and K. Hoshino, in *Molecular Sensors and Nanodevices*, edited by J. X. Zhang and K. Hoshino (William Andrew Publishing, Oxford, 2014) pp. 415–465.

[16] T. Billovits, P. Supancic, and B. Kaufmann, Open Ceramics **6**, 2666 (2021).

[17] C. Leach, Journal of the European Ceramic Society **21**, 2127 (2001).

[18] A. Rečnik, S. Bernik, and N. Daneu, Journal of Materials Science **47**, 1655 (2012).

[19] Versa, "FIB versa 3d product summary," (2015).

[20] L. A. Giannuzzi and F. A. Stevie, *Introduction to Focused Ion Beams: Instrumentation, Theory, Techniques and Practice* (2005).

[21] A. Schwartz, M. Kumar, B. Adams, and D. Field, *Electron backscatter diffraction in materials science* (2009) pp. 1–403.

[22] S. Suzuki, JOM **65**, 1254 (2013).

[23] K. Babinsky, R. De Kloe, H. Clemens, and S. Primig, Ultramicroscopy **144**, 9 (2014).

[24] D. J. Larson, T. J. Prosa, R. M. Ulfig, B. P. Geiser, and T. F. Kelly, *Local Electrode Atom Probe Tomography* (2013).

[25] W. Lefebvre-Ulrikson, F. Vurpillot, and X. Sauvage, *Atom Probe Tomography: Put Theory Into Practice* (2016).

[26] N. Dawahre, G. Shen, S. Balci, W. Baughman, D. Wilbert, N. Harris, L. Butler, R. Martens, S. Kim, and P. Kung, Journal of Electronic Materials **41**, 801 (2012).

[27] P. Supancic, "Results of investigations on Energy Varistors," Tech. Rep. (Materials Center Leoben, 2010).

[28] N. Ohashi, K. Kataoka, T. Ohgaki, I. Sakaguchi, and H. Haneda, Materials Transactions **50**, 1060 (2009).

[29] A. Cerezo, P. Clifton, M. Galtrey, C. Humphreys, T. Kelly, D. Larson, S. Lozano-Perez, E. Marquis, R. Oliver, G. Sha, K. Thompson, M. Zandbergen, and R. Alvis, Materials Today **10**, 36 (2007).

[30] J. Li, K. Tang, S. Yang, and D. Zhu, Ceramics International **47**, 19394 (2021).

[31] M. Matsuoka, Japanese Journal of Applied Physics **10**, 736 (1971).

[32] Z. . Wu, J. . Fang, D. Xu, Q. . Zhong, and L. . Shi, International Journal of Minerals, Metallurgy and Materials **17**, 86 (2010).

[33] S. Hamdelou and K. Guergouri, Journal of Ceramic Science and Technology **7**, 357 (2016).